ZnO – Yb_2O_3 composite optical ceramics: Synthesis, structure and spectral-luminescent properties

Elena Gorokhova, Olga Dymshits, Ivan Venevtsev, Liza Basyrova, Irina Alekseeva, Alexander Khubetsov, Mikhail Baranov, Marina Tsenter, Aleksander Zhilin, Sergey Eron'ko, et al.

Highlights

ZnO optical ceramics containing 0 – 2 wt% Yb are prepared by uniaxial hot pressing;
Yb ions form a cubic Yb_2O_3 phase located at the ZnO grain boundaries;
The ceramics exhibit a total transmittance up to 60% in the visible;
Absorption and photoluminescence of Yb^{3+} ions correspond to those in Yb_2O_3 crystals;
Addition of Yb affects the spectra and fastens the decay of X-ray induced luminescence

$ZnO – Yb_2O_3$ composite optical ceramics: Synthesis, structure and spectral-luminescent properties

Elena Gorokhova[1], Ivan Venevtsev[2], Olga Dymshits[1,*], Liza Basyrova[3], Irina Alekseeva[1], Alexander Khubetsov[1], Mikhail Baranov[4], Marina Tsenter[1], Aleksander Zhilin[5], Sergey Eron'ko[1], Eugenia Oreschenko[1], Faina Muktepavela[6], Karlis Kundzins[6] and Pavel Loiko[3]

[1] S.I. Vavilov State Optical Institute, 36 Babushkina St., 192171 St. Petersburg, Russia
[2] Peter the Great St. Petersburg Polytechnic University, 29 Polytechnic St., 195251 St. Petersburg, Russia
[3] Centre de Recherche sur les Ions, les Matériaux et la Photonique (CIMAP), UMR 6252 CEA-CNRS-ENSICAEN, Université de Caen Normandie, 6 Boulevard Maréchal Juin, 14050 Caen Cedex 4, France
[4] ITMO University, 49 Kronverkskiy Pr., 197101 St. Petersburg, Russia
[5] D.V. Efremov Institute of Electrophysical Apparatus, 196641 St. Petersburg, Russia
[6] Institute of Solid State Physics, University of Latvia, 8 Kengaraga St., LV1063 Riga, Latvia

Abstract: Zinc oxide optical ceramics containing 0 – 2 wt% ytterbium are prepared by uniaxial hot pressing of commercial oxides at 1150 and 1180 °C. The ceramics have the main crystalline phase of hexagonal wurtzite-type ZnO. Ytterbium ions do not enter the ZnO crystals but form a cubic sesquioxide phase of Yb_2O_3 located at the ZnO grain boundaries. Yb acts as an inhibitor for the ZnO grain growth. The ceramics exhibit transmittance up to 60% in the visible. Their transmission in the infrared is determined by the free charge carrier absorption. The Yb^{3+} ions are found in C_2 and C_{3i} sites in Yb_2O_3 crystals. Under X-ray excitation, the ceramics exhibit intense luminescence bands in the blue (near-band-edge emission) and green (defect emission) whose positions, intensities and decay times depend on the Yb content. Yb_2O_3 causes a redistribution of luminescence intensity in favor of the near-band-edge emission and fastens the emission decay.

Keywords: optical ceramics; zinc oxide; ytterbium sesquioxide; structure; luminescence.

1. Introduction

Zinc oxide (ZnO) is a direct wide band gap semiconductor. It has the wurtzite structure with a hexagonal lattice characterized by two interpenetrating sub-lattices of Zn^{2+} and O^{2-} ions, such that each zinc ion is surrounded by a tetrahedron of oxygen ions and vice versa. The non-centrosymmetric structure of ZnO is responsible for its piezoelectricity and pyroelectricity. Unique optical and luminescent properties of zinc oxide are coupled with high chemical stability and radiation tolerance, eco-friendly characteristics, high biocompatibility, low toxicity and low-cost [1-3]. ZnO materials, both undoped and doped with different metal ions are used as photocatalysts, scintillators, in blue and UV light emitting devices, plasma displays, phosphors in fluorescencent lamps for lighting applications, solar cells and in biological labeling. ZnO materials doped with rare earth (RE) oxides are fabricated to obtain new properties that do not exist in pure ZnO and to enhance the photocatalytic and antibacterial activity. The RE doped ZnO appears promising for development of multifunctional materials with coexisting semiconducting, optical, and electromechanical properties [3-5].

ZnO can be produced in the form of single crystals, ceramics, nanopowders of different shapes, quantum dots and films [1]. ZnO optical ceramic is an alternative to single crystals, growing of which is a laborious and time-consuming process [3]. It is a challenging task to produce transparent ceramics from non-cubic ZnO crystals, and there are just a few research groups involved in this activity [6-8]. ZnO-based ceramics are obtained from ZnO powders using uniaxial hot pressing (HPing) [6,7] or spark plasma sintering [6,8,9]. Uniaxial HPing was successfully applied for fabrication of transparent ZnO ceramics with fascinating scintillating properties [7,10]. Undoped ZnO [7,10], ZnO:Zn [11], ZnO:Ga [10,12-16] and ZnO:In ceramics as scintillating materials have been developed so far [14,17].

Recently, we prepared Er-containing ZnO optical ceramics and evaluated their structure and spectral-luminescent properties [18,19]. We revealed that Er^{3+} ions do not enter the ZnO structure but rather form cubic crystals of Er_2O_3 and also locate at the ZnO grain boundaries.

The spectroscopy of Yb^{3+} ions in different hosts is intensively studied because of broadband emission of these ions around 1 μm. The Yb^{3+} ion has a simple energy level diagram: there is only one excited state $^2F_{5/2}$ which is separated from the ground state $^2F_{7/2}$ by an energy gap of 10000 cm^{-1} [20], so that energy transfer upconversion and excited state absorption are avoided eliminating the energy losses. The excitation of Yb^{3+} ions·by laser diodes is also possible [20].

Various ZnO materials doped with ytterbium ions were previously developed and studied, i.e., quantum dots [21], nanomaterials [22-31], films [33-43], microspheres [44] and ion implanted single crystals [45,46].

The authors of all these studies mentioned that an addition of ytterbium ions modifies the structure, texture and properties of ZnO materials. In a series of publications [24,25,32-34,39,41,43-45], the authors did not register any crystalline phase other than ZnO by the X-ray diffraction (XRD) analysis, which led them to conclusion that Yb^{3+} ions enter into the ZnO lattice. Any amount of Yb in other phases was claimed to be below the detection limit of the XRD analysis [41]. In [33], Balestrieri *et al.* pointed out that in Yb-doped films, the lattice parameter *c* of ZnO increases continuously with doping up to 2%, suggesting that the amount

of Yb substituting Zn^{2+} ions increases continuously, and the solubility limit of Yb in ZnO is not reached. Guziewicz *et al.* [36] suggested that after implantation, the ytterbium ions are mainly in the Yb^{2+} state substituting Zn^{2+} ions and they are transformed to the trivalent state as a result of annealing, which substantially reduces substitutional fraction of Yb atoms due to diffusion from substitutional to interstitial positions where Yb ions are in *the optically active Yb^{3+} state*.

In another series of studies, a different approach to the structure of Yb-doped ZnO materials was suggested [23,26,30,31,35,42]. The authors proposed that the difference in the ionic radii and valence states between Zn^{2+} and Yb^{3+} ions prevents entering the ZnO structure by these ions. The trivalent RE ion is difficult to be doped into the ZnO lattice and thus most of the RE^{3+} ions were found either located at the surfaces or at the grain boundaries of ZnO crystals [47-50]. Though XRD analysis sometimes was not able to detect an additional phase of Yb_2O_3, the electron microscopy data revealed Yb_2O_3 nanoparticles, forming the Yb_2O_3-ZnO interface [23,30]. In [28], based on the XRD study, Cerrato *et al.* came to conclusion that among the rare-earth oxides, only cerium ions create a separate oxide phase, while all the other ones are probably inserted in the ZnO matrix, however, in [30,31], Cerrato *et al.* demonstrated that ytterbium ions do not form extrinsic defects entering in ZnO lattice but they form Yb_2O_3 nanoparticles stabilized at the ZnO surface. Shalygina *et al.* [26] demonstrated that thermally annealed nanocomposites with Yb atomic content of 0.5–6% consist of Yb_2O_3 nanocrystals, which decorate the surface of ZnO nanoparticles.

The ZnO materials were doped not only with ytterbium oxide, as we described before, but they were codoped with ytterbium oxide and several other RE oxides simultaneously [512-53]. There also exist two different approaches to the description of structure of these materials. In [51], Balakrishna *et al.* suggested that non-varying hexagonal structure and a lack of any impurity peaks in the XRD patterns mean that Eu and Yb atoms were homogeneously distributed within the ZnO lattice. In [52], the authors proved the formation of nanocomposites of ZnO with Yb_2O_3 and Pr_2O_3.

There is another group of materials based on ZnO, namely, the ZnO varistors, which are the materials that are predominantly used to protect the electric circuits in both low and high voltage applications against surges. They contain different dopants, sometimes including Yb ions [53]. It was demonstrated [54] that in varistors, the RE ions do not enter the ZnO crystals. When the concentration of RE_2O_3 is less than 0.5 mol%, most of the RE^{3+} cations are segregated at the grain boundaries. When the amount of RE_2O_3 is more than 0.5 mol%, they participate in formation of the new crystalline phase located at the grain boundaries [54].

Rahman *et al.* [27] successfully fabricated ZnO/Yb_2O_3 sensors. Shestakov *et al.* [23] prepared ZnO/Yb_2O_3 nanocomposites for energy transfer luminescence and have reported excellent results for solar cells. Novel ZnO based tri-phase heterostructured ZnO–Yb_2O_3–Pr_2O_3 nanocomposite materials to enhance the photocatalytic and antibacterial activity of ZnO have recently been fabricated [52].

Ytterbium-doped ZnO nanostructures and films demonstrate efficient energy transfer between the defect states in the ZnO structure and the dopant Yb^{3+} ions [23], making them promising for application as down-conversion layers for enhanced solar cells [33]. The

mechanisms that govern the energy transfer were discussed in the literature. In [30], Cerrato *et al.* suggested the formation of an Yb_2O_3-ZnO heterojunction in a similar way as it was proposed in their previous study devoted to the CeO_2/ZnO heterojunction [47]. The experimental results were explained by assuming energy transfer from the photoexcited zinc oxide nanocrystals to ytterbium oxide nanoparticles on their surface. Shestakov *et al.* [23] explained the energy transfer from the ZnO nanocrystals (absorption range from 250 to 400 nm) to Yb^{3+} ions (emission range from 950 to 1100 nm) by a model considering the quantum cutting effect. In [42], Kim *et al.* also suggested that the energy-transfer process from the ZnO host to Yb_2O_3 was followed mainly by a quantum cutting process, even though there was no substitution of Yb into the Zn sites. The obtained results indicate possible applications of Yb-doped zinc oxide nanostructures in optoelectronics devices and as infrared biomarkers.

In the present work, the effect of Yb doping level on the structure, optical and spectral-luminescent properties of ZnO optical ceramics was studied for the first time, to the best of our knowledge.

2. Experimental

The undoped and Yb-doped ZnO optical ceramics with the Yb concentration of 0.2, 0.4, 0.6, 0.8, 1.0 and 2.0 wt% were fabricated from commercial reagent-grade powders of zinc oxide ZnO (purity: 3N, Zinsa, Peru) and ytterbium oxide, Yb_2O_3, (purity 3N) without any further purification treatment. We used two different batches of ytterbium oxide from the same Russian supplier bought at different times and denoted as batches No. 1 and No. 2. The weighted portions of ZnO and Yb_2O_3 were thoroughly mixed. The ceramics were prepared by the uniaxial HPing in a high-temperature vacuum furnace at the temperatures of 1150 °C and 1180 °C. The undoped ZnO ceramic and ceramics containing 0.2 - 1.0 wt% Yb (the batch of Yb_2O_3 No. 1) were prepared at the temperature of 1150 °C. All ceramics fabricated at 1150 °C except for the ZnO:1 wt% Yb one were homogeneous, see Fig. 1. With the purpose to fabricate heavily doped ceramics with better homogeneity, we increased the HPing temperature to 1180 °C. By this time, we have consumed all Yb_2O_3 reagent from the batch No. 1, so that we had to prepare ceramics doped with 1.0 and 2.0 wt% Yb at the temperature of 1180 °C using Yb_2O_3 from the batch No. 2. These ceramics were homogeneous, see Fig. 1. To compare the properties of ceramics fabricated using different batches of Yb_2O_3, the ceramic doped with 1 wt% Yb and fabricated using Yb_2O_3 from the batch No. 2 was also sintered at 1150 °C. This ceramic also was homogeneous.

Both sides of the as-sintered ceramic disks were mirror polished using diamond slurry. After polishing, the disks had a diameter of 25 mm and a thickness of about 0.5 mm. The undoped ceramic was of yellow-green color. With Yb^{3+} doping, the color changed to grey. The obtained transparent undoped and Yb-doped ZnO ceramics are shown in Fig. 1.

The XRD patterns of ceramic disks were measured using a Shimadzu XRD-6000 diffractometer with a Ni-filtered Cu $K_{\alpha 1}$ radiation (1.54056 Å). The samples were scanned continuously according to a "standard mode" (continuous scan, sampling pitch: 0.02°, preset time: 0.6 s) in the 2θ range between 30° and 120°. This angular range was chosen because the ZnO pattern has no diffraction peaks at 2θ degrees smaller than 30°. To check whether crystals

of Yb_2O_3 were formed during sintering, additional XRD patterns were recorded in a "special mode" (fixed time scan, sampling pitch: 0.01°, preset time: 100 s) in an angular range of 2θ = 29.0-30.3°, where the main diffraction peak of cubic Yb_2O_3 is located. The Rietveld refinement was performed using the Maud software [55].

For evaluating the preferred orientation of ZnO samples, the texture coefficient $T_c(hkl)$ was used. It was calculated by the following equation:

$$T_c(hkl) = \frac{I(hkl) / I_0(hkl)}{(1/N)\left[\sum_N I(hkl) / I_0(hkl)\right]}, \quad (1)$$

where (*hkl*) is the crystalline plane, *I* is the measured XRD intensity, I_0 is the standard intensity of randomly oriented crystals according to a reference JCPDS XRD pattern and *N* is the number of diffraction peaks [56]. It is evident from Eq. (1) that T_c is close to unity for randomly oriented crystals, and it is greater than 1 when a certain (*hkl*) plane is preferentially oriented.

The Raman spectra of ceramics were measured using a confocal Raman microscope (Renishaw inVia) with a Leica ×50 objective (N.A. = 0.75). The excitation wavelength λ_{exc} was 514 nm (Ar^+ laser line). The spatial resolution was about 2 cm^{-1}. Each spectrum was averaged over 30 acquisitions with a duration of 10 s.

The transmission electron microscope (TEM) images were acquired using a Tecnai GF20 (Zeiss AG, Oberkochen, Germany) microscope for the morphological investigation of the commercial ZnO powder used for the ceramic preparation, and for the estimation of the ZnO crystal sizes in this powder. The morphology of ceramics was characterized by scanning electron microscopy (SEM) using Carl Zeiss EVO, TESCAN LYRAS and Carl Zeiss MERLIN microscopes. For this study, the surface of ceramics was preliminary etched in a mixture of hydrochloric and hydrofluoric acids. The same MERLIN microscope equipped with an Inca Energy X-Max analyzer was employed for energy dispersive X-ray (EDX) based element mapping. The grain size distribution was analyzed with the ImageJ software.

The total transmittance spectra in the spectral range of 300 – 1200 nm were measured using a SPECORD 200 PLUS spectrophotometer coupled with an integrating sphere. The transmission spectra in the spectral range of 1.3 – 5.0 μm and the reflection spectra in the spectral range of 2 – 25 μm were measured with an IR Fourier spectrometer FSM 1201. The optical absorption spectra at 300 – 3300 nm were measured using a spectrophotometer Shimadzu UV-3600 with a spectral resolution of 1 nm (0.2 nm for the range of 890 – 1050 nm). The luminescence spectrum of Yb^{3+} ions was measured using an optical spectrum analyzer (OSA, Ando AQ6315-E) and a Ti:sapphire laser as an excitation source. Low temperature (LT, 10 K) absorption and luminescence spectra of Yb^{3+} ions were measured using an APD DE-202 closed-cycle cryo-cooler equipped with an APD HC 2 Helium vacuum cryo-compressor and a Laceshore 330 temperature controller.

The X-ray induced luminescence (XRIL) spectra were recorded in the reflection geometry upon continuous excitation by an X-ray tube with a tungsten anode (40 kV, 10 mA, the distance to the sample: 3 cm). The spectra were recorded with the MDR-2 monochromator and a photon counting head Hamamatsu H8259-01. The decay kinetics of X-ray luminescence

were recorded using a pulsed X-ray setup with a pulse duration of ~1 ns at a voltage of 30 kV and a current amplitude of 500 mA.

3. Results and discussion

3.1. Structural and morphological characterization of ceramics

3.1.1. XRD analysis

The XRD study of the commercial reagent-grade ZnO powder revealed the characteristic pattern of ZnO without any contaminations.

A typical diffraction pattern of 2 wt% Yb-doped ZnO ceramic is shown in Fig. 2(a). It demonstrates diffraction peaks corresponding to all the planes of the wurtzite hexagonal phase of ZnO, sp. gr. $P6_3mc$ – C^4_{6v}, No. 186, ISDD card No. 5-0664. The calculated unit cell parameters for the ZnO ceramics are listed in Table 1. When comparing them with the literature data (a = 3.249 Å, c = 5.205 Å, ISDD card No. 5-0664), one may conclude that within the experimental error (±0.003 Å), the parameters of the ZnO phase are not influenced by the addition of ytterbium oxide. It means that Yb^{3+} ions do not enter the structure of ZnO crystals in the ceramics. Since ytterbium ions do not enter the ZnO crystals, they can be adsorbed on certain planes of ZnO as well as form their own crystalline phase of Yb_2O_3.

Indeed, the crystals of Yb_2O_3 are detected in the XRD pattern of the ceramic containing 2 wt% Yb, where weak diffraction peaks of Yb_2O_3 are found at the angles 2θ = 49.4° and 58.6°, Fig. 2(a). The crystals of Yb_2O_3 (ytterbium sesquioxide or ytterbia) have a cubic bixbyite-type structure (sp. gr. $Ia\bar{3}$ - T^7_h, No. 206, a = 10.441 Å, ISDD card No. 84-1879). The strongest diffraction peak of Yb_2O_3 with the Miller's indices (hkl) = (222) is located at 2θ = 29.63°. This peak was detected in the "special mode", Fig. 2(b).

The variation of the diffraction intensity of the (222) diffraction peak of Yb_2O_3 with the concentration of Yb in the ZnO ceramics is shown in Fig. 2(c). The intensity increases linearly with an increase in the Yb concentration from 0.2 to 0.8 wt% (for ceramics prepared at the same temperature of 1150 °C using Yb_2O_3 from the batch No. 1), which indicates an increase in the Yb_2O_3 crystal fraction in ceramics with increasing the Yb_2O_3 content in the initial load. This finding agrees with the previous studies [23,26,30,31,35,42], where it was pointed out that Yb ions did not incorporate into the ZnO host because of the large difference in the ionic radii and the oxidation states of Zn^{2+} and Yb^{3+} cations [42]. In [49], Bai *et al.* also indicated that for ZnO:Er,Yb nanocrystals, the peak intensity of the Yb_2O_3 crystalline phase increases with increasing the concentration of Yb^{3+} ions.

A change of the source of Yb_2O_3 and simultaneous increase in the HPing temperature by 30 °C, from 1150 to 1180 °C, leads to a disproportional increase in the intensity of the (222) diffraction peak of Yb_2O_3, Fig. 2(c). To understand the possible reason of this increase (namely, the change of the source of Yb_2O_3 or the change of the HPing temperature or both of them), we compared the intensities of the (222) diffraction peak in the XRD patterns of the ZnO:1 wt% Yb ceramic prepared from different batches of Yb_2O_3 at different temperatures. The intensity of the (222) diffraction peak of Yb_2O_3 in the XRD pattern of 1 wt% Yb doped ceramic fabricated at 1150 °C is similar to that for ceramic fabricated at 1180 °C (using Yb_2O_3 from the same batch No. 2). However, this intensity is higher than that for the ceramic

fabricated at 1150 °C using Yb_2O_3 from the batch No. 1. It means that the influence of the source of ytterbium oxide on crystallization of Yb_2O_3 is more pronounced than the influence of the HPing temperature.

3.1.2. Raman spectroscopy

Figure 3 shows unpolarized Raman spectra of ZnO optical ceramics, undoped and doped with 0.2 – 1.0 wt% Yb (Yb_2O_3 from batch No. 1) and prepared at 1150 °C. For wurtzite-type ZnO, which belongs to the sp. gr. C^4_{6v}, there are two formula units in the primitive cell. At the center of the Brillouin zone (Γ point), the group theory predicts the following irreducible representations: $\Gamma_{opt} = A_1 + E_1 + 2E_2 + 2B_1$. The polar A_1 and E_1 modes are both Raman and infrared active, the E_2 modes (E_2^{low} and E_2^{high}) are nonpolar and Raman active only while the B_1 modes are silent [57]. One of the most intense modes in the Raman spectrum of ZnO is a very narrow peak E_2^{low} at ~100 cm^{-1}, ascribed to vibrations of the zinc sublattice in ZnO [58]. Another intense Raman mode E_2^{high} at~439 cm^{-1} is assigned to oxygen vibrations [58].

All characteristic vibrations of ZnO with wurtzite structure [57-60] are observed in the Raman spectra of ZnO ceramics at 99, 204, 331, ~378, 409, 437, 484, 536, 584, 663, 1096 and 1153 cm^{-1}. A detailed analysis of the Raman spectra of ceramics allowed us to list the Raman-active frequencies of the ZnO crystals observed in the studied materials in comparison with the literature, see Table 2.

Though the position of Raman bands is nearly independent on the Yb doping level, Fig. 3(a), we tried to find the signs of Yb_2O_3 Raman modes in the spectra of Yb-doped ZnO ceramics. According to [61], the Raman modes of Yb_2O_3 are observed at 94, 118, 133, 143, 308, 360, and 612 cm^{-1}. According to [62], they are located at 269.6, 301.9, 337.5, 363.8, and 613.5 cm^{-1} and demonstrate a broad shoulder in the range of 400–545 cm^{-1}. These modes can be divided into two groups: in the range above 300 cm^{-1}, internal vibrations of [YbO_6] octahedrons are observed, whereas in the range below 200 cm^{-1}, the translational motions of these octahedrons and the Yb ions are dominant [63]. In the spectra of Yb-doped ZnO ceramics, the intense Raman modes of Yb_2O_3 that should locate at 94 and ~360 cm^{-1} [61,63] can overlap with the modes characteristic for ZnO and observed at 99, 337.5, and ~378 cm^{-1}. As a result, the peak at ~378 cm^{-1} is enhanced in the spectra of Yb-doped ZnO ceramics. According to Fig. 3(b), with the introduction of ytterbium oxide into the ZnO ceramic and with the increase in its doping level up to 1 wt%, the band with a maximum at 378.4 cm^{-1} continuously shifts to lower frequencies with a formation of a “tail” in the region of ~365 cm^{-1}. Note that there is no shift of the Raman band of ZnO with a maximum at 331 cm^{-1}. The rise in the Raman spectrum of Yb-doped ceramics in the region of 200–600 cm^{-1} with increasing the Yb_2O_3 content can also be explained by the contribution of the wide shoulder of Raman modes of Yb_2O_3 in the spectral range of 400–545 cm^{-1}.

3.1.3. Texture characterization

The uniaxial pressing conditions applied for the formation of optical ceramics inevitably lead to texture appearance, i.e., to a predominant orientation of crystal grains. The contribution of different planes of ZnO crystals to the formation of texture was estimated by the texture

coefficient, see Eq. (1). The reflections from the planes of a hexagonal prism have Miller's indices (100) and (110), those from a pedion - (002), and those from a hexagonal pyramid - (101) and (102).

For the undoped ZnO ceramic sample, the texture is dominated by the prism planes (100) and (110) of the ZnO crystals, Table 3. For the ZnO:Yb ceramics fabricated at 1150 °C using Yb_2O_3 from the batch No. 1, the texture is determined by the preferential orientation of the faces of the pedion (002) and the sharp pyramid (102), while the prism faces are arranged statistically, Table 3. The texture of the samples increases with increasing the Yb_2O_3 concentration. The sharp pyramid with (*hkl*) = (102) has a higher texture coefficient than the shallow one with (*hkl*) = (101), for which the texture coefficient is about 1.10 independently of the Yb_2O_3 concentration.

Quite a different texture was observed in other ZnO samples also doped with 1.0% Yb and prepared at 1150 °C and 1180 °C using Yb_2O_3 from the batch No. 2. In these samples, the texture components are different from those found before. For the ceramic containing 1.0 wt% Yb and prepared at 1150 °C, the prism planes with (*hkl*) = (100) and (110) and the shallow pyramid (101) with texture coefficients of 1.99, 1.73, and 1.35, respectively, dominate. For the ceramic of the same composition prepared at 1180 °C, the same simple forms with slightly lower texture coefficients appear with T_c of 1.59, 1.32 and 1.21, respectively. We supposed that different batches of the Yb_2O_3 reagent could contain different uncontrollable impurities which may influence the texture of ceramics. To verify this idea, we recorded the XRD patterns of Yb_2O_3 from these two batches, as shown in Fig. 4. Indeed, the XRD patterns of the reagents are different. The Yb_2O_3 reagent from the batch No. 1 contains all the diffraction peaks of Yb_2O_3, ISDD card No. 84-1879, and many additional peaks attributable to some organic salts of ytterbium, probably, to ytterbium citrates, as citrates are often used as eluants for the separation of rare-earth ions [64]. The XRD pattern of the same reagent heat-treated at 400 °C for 2 h demonstrated only peaks of Yb_2O_3, which proves that additional peaks in the XRD pattern belong to organic compounds that decompose during the heat-treatment and as one may expect during the ceramic preparation. The XRD pattern of Yb_2O_3 from the batch No. 2 contains only the diffraction peaks of ytterbium oxide, ISDD card No. 84-1879. This pattern does not contain any signs of contamination. Thus, the character of texture and the values of the texture coefficients of ZnO ceramics mainly depend not on the Yb_2O_3 doping level and the HPing temperature. It is quite amazing that the texture characteristics of ZnO:Yb ceramics are sensitive to uncontrollable impurities in the Yb_2O_3 reagent. The dopants might act as structure driving agents through selectively adsorbing onto ZnO crystalline planes, which will prevent further deposition of Zn species at those surfaces [25]. Our results agree with the previous work [25] which documented the change of the shapes of the nanostructures from nanorod-like to nanoplate-like induced by doping of ZnO with Er and Yb.

3.1.4. Morphological characterization

Figure 5 depicts a TEM image of the commercial reagent-grade ZnO used for the ceramic preparation. The ZnO powder consists of small spherical and prismatic particles (so-called

nanorods), as well as aggregates of undefined shape. The particle size ranges from (10 - 50)×50 nm up to (200 - 500)×100 nm. The crystals in the ZnO powder are randomly oriented, aggregated and agglomerated.

The surface morphology of ceramics was characterized by SEM. Figure 6 shows typical SEM images of an etched polished surface of the 1.0% Yb-doped (Yb_2O_3 from batch No. 1) transparent ZnO ceramic as an example. The sintering of powders occurs along thermodynamically favorable crystal planes. The micrograph demonstrates grain surfaces with different orientations. They are the faces of the prism and pedions with characteristic growth hillocks in the form of hexagonal pyramids. The microstructure of the ZnO:1.0 wt% Yb ceramic presented in Fig. 6 is characteristic of all the ceramics under study. The sizes of the resulting grains are not uniform. It is reasonable to assume that larger grains are built of ZnO, as the HPing temperature of 1150 °C corresponds to $0.81\times T_{mZnO}$, where T_{mZnO} is the ZnO melting point, so that the diffusion processes of recrystallization are accelerated. The adhered small grains can be attributed to ytterbium oxide crystals, for which the HPing temperature is only $0.5\times T_{mYb2O3}$, which is sufficient only for surface interactions and the formation of small grains.

The variation of the Yb_2O_3 concentration, the source of the Yb_2O_3 reagent and the HPing temperature do not influence the surface morphology of ZnO crystals.

Note that synthetic ZnO single crystals demonstrate similar morphology [65]. The hexagonal prism, the pedion, and the hexagonal pyramid are simple forms characteristic for hexagonal ZnO crystals belonging to the 6*mm* point group [66,67]. The hexagonal pyramid in this case is a growth pyramid located on the as-grown zincite {0001} face [68,69] and it can be considered as a pseudomorph [70]. The growth pyramids are often found in crystals with a hexagonal close-packed structure. In [67], hexagonal growth hillocks were observed on the fast growing positive pedion face {0001} of the ZnO single crystal obtained via hydrothermal synthesis. Small cone-shaped growth hillocks were also found on the negative pedion face $\{000\bar{1}\}$ [71].

The average ZnO grain size was determined from the SEM images of ceramics fabricated at the temperatures of 1150 and 1180 °C, see Fig. 7(a) showing the typical grain size distribution for the ZnO:0.8 wt% Yb ceramic. Figure 7(b) shows the dependence of the average ZnO grain size on the Yb concentration. The addition of 0.2 wt% Yb significantly (almost 4 times, from 23.0 to 6.6 μm) reduces the average grain size of ZnO ceramics prepared at 1150 °C. With increasing the Yb content from 0.2 to 0.4 wt%, the average grain size decreases to 4.0 μm, while further increase of the Yb content up to 1.0 wt% practically does not affect the grain size. The RE oxides can act as grain growth inhibitors for ZnO grains during sintering [28,30,31,42,43,72]. The decrease of the ZnO grain size with increasing the concentration of the doping rare-earth ions was well documented [54,73,74] and connected with segregation of rare-earth ions at the grain boundaries, which inhibits the growth of ZnO grains. Therefore, the decrease of the ZnO grain size in ceramics with the addition of Yb can be associated with adsorption of Yb^{3+} ions at the grain boundaries. The lack of the effect of higher Yb concentration on the grain size can be related to crystallization of an independent crystalline

phase of Yb_2O_3, see Fig. 2(b), which reduces the effective concentration of ytterbium ions localized at certain grain boundaries and interacting with the ZnO crystals.

3.1.5. The microstructure and compositional analysis of the ZnO and ZnO:Yb ceramics

The microstructure and elemental composition of ceramics were evaluated by SEM coupled with EDX analysis. The results for undoped and Yb-doped ZnO ceramics are shown in Fig. 8(a-d) and Fig. 9(a-f), respectively. According to Fig. 8, the undoped ZnO sample consists of zinc and oxygen ions uniformly distributed over the sample. The regions with different microstructures are composed of the same elements in similar proportion. According to the EDX data, the ZnO ceramic is oxygen deficient, which can be connected with its fabrication via HPing in vacuum. Figure 9(d-f) shows the surface element mapping (Zn, O and Yb) for the 1.0 wt% Yb-doped ZnO ceramic fabricated at 1180 °C. The EDX mapping clearly reveals a two-phase structure of the ceramic. In the ceramic, there exist areas ranging in size from a few to tens of μm, containing ytterbium oxide. These regions do not contain Zn atoms. We performed the SEM study of fracture surfaces of ZnO:Yb ceramics to determine the arrangement and location of Yb_2O_3 crystals in the ZnO ceramics. The sizes of Yb_2O_3 crystals are much smaller than those of the ZnO grains due to a significant difference in their melting temperatures. The recrystallization temperature is insufficient for the growth of large crystals of Yb_2O_3 with higher melting temperature. The areas of ytterbium oxide have a broad size distribution. We found out that the Yb_2O_3 crystals are formed at different sites of the ZnO ceramic, most often at the grain boundaries, and between the ZnO planes. They are irregularly distributed in the ceramics while a very small fraction of ytterbium ions is located at the grain surfaces of zinc oxide. These data prove that ytterbium ions are located at the ZnO grain boundaries (GB) and form the Yb_2O_3 crystals. The Yb_2O_3 crystals located at the GBs of ZnO grains have sufficient adhesion to ZnO, which indicates a good interaction (interdiffusion) at the GBs of these oxides. We can assume the leading role of the special (nonequilibrium) state of the electronic structure of the boundaries in the processes of interaction and transfer of excitation energy from ZnO to Yb^{3+} ions, which leads to an increase in the near-band-edge emission intensity (see Section 3.2.3).

3.2 Optical properties of ZnO:Yb ceramics

3.2.1 Transmission, reflection and absorption spectra

The transmission and reflection spectra of ceramics are shown in Fig. 10(a-c). The doping with ytterbium ions leads to a pronounced non-monotonous change in the absolute value and spectral behavior of transparency of ZnO ceramics. The ceramic doped with 0.2 wt% Yb demonstrates the highest transparency exceeding that of the undoped ZnO ceramic. Its total transmittance is higher than 60% at the wavelengths of 500 – 1300 nm, see Fig. 10(a). The transmittance spectra of undoped and 0.2 wt% Yb-doped ZnO ceramics in this spectral range are almost flat. The shape of transmittance curves changes for ceramics doped with 0.4 – 0.8 wt% Yb as the maximum transmittance reduces to about 40% and the transmittance decreases in the infrared. The ceramic doped with 1 wt% Yb (the batch No. 1) and hot pressed at 1150 °C is inhomogeneous, as evidenced by different transmittance spectra for different areas of this

sample. The use of Yb_2O_3 from the batch No. 2 made it possible to obtain homogeneous ZnO:1.0 wt% Yb ceramics with increased transmittance in the region of 500-1000 nm both at 1150 °C and 1180 °C. The maximum transmittance of these ceramics is superior to that of the 0.8 wt% Yb-doped ceramic fabricated at the temperature of 1150 °C. The transmission curves of the homogeneous ceramics doped with 1.0 and 2.0 wt% Yb (Yb_2O_3 from the batch No. 2) are flatter than those for ceramics containing 0.4 -1.0% Yb (Yb_2O_3 from the batch No. 1).

All the transmission curves of Yb-doped ZnO ceramics clearly reveal the absorption band of Yb^{3+} ions at ~1 μm due to the $^2F_{7/2} \rightarrow {}^2F_{5/2}$ electronic transition [20]. The absorption at these wavelengths gradually increases with an increase in the ytterbium concentration.

The short-wavelength transparency edge of Yb-doped ceramics is located at about 390 nm. The transmission spectra of ZnO:Yb ceramics (with the exception of that doped with 0.2 wt% Yb) demonstrate the maximum in the visible. The position of the long-wavelength edge depends on the concentration of ytterbium ions, the source of Yb_2O_3 (i.e., uncontrollable impurities) and the fabrication temperature of ceramics, Fig. 10(b). For the ZnO:0.2 wt% Yb ceramic, it is located at 4.1-4.2 μm, i.e., at slightly longer wavelengths than that for the undoped ceramic. For the 1.0 wt% Yb-doped ceramic (Yb_2O_3 from batch No. 1) with the HPing temperature of 1150 °C, it is found at ~1.7 μm. For ceramics doped with 0.4 – 0.8 wt% Yb, the long-wavelength edge is in the range of 2.0–2.5 μm. The heavily doped ceramics (1 – 2 wt% Yb) fabricated at 1180 °C have the same position of this transparency edge, 2.5 μm. For the 1.0 wt% Yb-doped ceramic (Yb_2O_3 from batch No. 2) obtained at the HPing temperature of 1150 °C, it is found at ~ 2.6 μm.

The infrared absorption measurements of ZnO single crystals demonstrate absorption in the 3–10 μm spectral region assigned to free carrier absorption [75-78]. The observed decrease in the transmittance and the shift of the long-wavelength transparency edge to lower wavelengths in Yb-doped ceramics as compared to the undoped ZnO one indicates an increase in the concentration of free carriers with increasing the concentration of ytterbium ions. The free carrier concentration N (in cm^{-3}) was determined using the following equation [79]:

$$N = \frac{7.24 \times 10^{20}}{\lambda_{min}^2}\ , \qquad (2)$$

where λ_{min} (in μm) is the wavelength corresponding to the minimum reflectance in the infrared reflectance spectrum. The calculated N value for the undoped ZnO ceramic is 3.13×10^{18} cm^{-3}, while for the Yb-doped samples, it increases with increasing the Yb concentration: for ceramics fabricated at 1150 °C, an increase in the Yb content from 0.2 to 0.8-1.0 wt% causes an increase in the free carrier concentration N from 3.97×10^{18} cm^{-3} to 11.9×10^{18} cm^{-3}. Note that all these ceramics were obtained using Yb_2O_3 from the batch No. 1.

For the 1.0 wt% Yb-doped ZnO ceramic obtained at the temperature of 1150 °C using Yb_2O_3 from the batch No. 2, the free carrier concentration is 6.6×10^{18} cm^{-3}, which is significantly lower than that for a similar ceramic prepared using Yb_2O_3 from the batch No. 1 (11.9×10^{18} cm^{-3}). It means that the free carrier concentration in ZnO:Yb ceramics depends on the source of ytterbium oxide, which confirms our supposition about the role of uncontrollable impurities in Yb_2O_3 from the batch No. 1. The use of Yb_2O_3 with less impurities (batch No. 2) leads to a decrease in the number of free charge carriers.

An increase of the HPing temperature by 30° results in a decrease of the free carrier concentration from 6.6×10^{18} cm^{-3} to 5.29×10^{18} cm^{-3} for the ceramics doped with 1.0 wt% Yb (Yb_2O_3 from the batch No. 2). For the ceramics doped with 2.0 wt% Yb and prepared at 1180 °C, *N* is again increased to 8.02×10^{18} cm^{-3}.

According to the absorption spectra of ZnO:Yb ceramics fabricated at 1150 °C using Yb_2O_3 from the batch No. 1, cf. Fig. 11(a,b), the absorption edge of ceramic samples is located in the violet spectral region, at 388-397 nm, slightly shifting towards longer wavelengths with increasing the Yb concentration, Fig. 11(b). The undoped ZnO ceramic has the lowest optical losses in the spectral range of 400-1000 nm. The absorption in this spectral region increases with increasing the Yb content. In the spectral range of 1000–3300 nm, the ZnO:0.2 wt% Yb ceramic is the most transparent one. At these wavelengths, a gradual increase in absorption is observed with the formation of an infrared absorption band. The position of the short-wavelength edge of this band experiences a shift to shorter wavelengths with an increase of the Yb concentration. This band was previously attributed to free carrier absorption, see Fig. 11. The absorption spectra of the ZnO: 1 wt% Yb ceramics fabricated at 1150 °C using Yb_2O_3 from the batches No. 1 and No. 2 are shown in Fig. 12(a). A pronounced difference in the position of the short-wavelength edge of the infrared absorption band is attributed to uncontrollable impurities in the Yb_2O_3 reagent.

3.2.2 Spectroscopy of Yb^{3+} ions

The absorption band of Yb^{3+} ions is located at 900 – 1000 nm, see Fig. 11(c). The most intense peak at 976 nm is due to the so-called zero phonon line (ZPL) transition between the lowest Stark sub-levels of two multiplets, while the weaker peaks at shorter wavelengths, at 903, 932 and 948 nm, are due to transitions to higher-lying sub-levels of the excited state ($^2F_{5/2}$). The assignment of these peaks can be done using the previously reported crystal-field splitting for Yb^{3+} ions in the cubic Y_2O_3 single crystal [20]. The Beer's law, i.e., a linear dependence between the concentration of Yb^{3+} ions and the absorption coefficient of ceramics at the ZPL wavelength (after subtracting the background losses), is fulfilled, see Fig. 11(d). It indicates that with increasing the Yb concentration under the same HPing temperature, new species do not appear, which allows us to conclude that the distribution of ytterbium ions between the ZnO grain boundaries and ytterbium oxide crystals is almost independent of the Yb^{3+} concentration.

The effect of increasing the HPing temperature from 1150 to 1180 °C on the absorption spectra of ZnO:Yb ceramics was studied by fixing the doping level to 1 wt% Yb (Yb_2O_3 from the batch No. 2), see Fig. 12(a,b). An increase in the sintering temperature by 30° has no influence on the position of the UV absorption edge and absorption in the visible, however, there is a significant shift of the infrared absorption edge toward shorter wavelengths and some increase in the absorption of Yb^{3+} ions. Note that according to Fig. 2(c), the fractions of Yb_2O_3 crystals in the ZnO:1.0 wt% Yb ceramics fabricated at 1150 °C and 1180 °C are similar. Thus, this increase in the absorption intensity of Yb^{3+} ions can be assigned to a redistribution of Yb^{3+} ions between the grain boundaries of ZnO and Yb_2O_3 crystals.

The absorption spectra of ZnO:Yb ceramics doped with 1.0 and 2.0 wt% Yb and fabricated at 1180 °C, Fig. 12(a,b), again demonstrate the applicability of the Beer's law, cf. Fig. 11(d), which implies that the distribution of Yb^{3+} ions between the ZnO grain boundaries and Yb_2O_3 crystals depends on the temperature of HPing of ceramics.

A typical spectrum of photoluminescence (PL) of Yb^{3+} ions in a ZnO:2 wt% Yb ceramic is shown in Fig. 13(a). The shape of the PL spectra of Yb^{3+} ions is nearly independent of the Yb content and the HPing temperature. The spectrum is characteristic for Yb^{3+} ions in the cubic sesquioxide phase and is related to the $^2F_{5/2} \rightarrow {}^2F_{7/2}$ transition [20]. The main peak at 976.4 nm corresponds to the ZPL transition in emission. Other prominent peaks appear at 1033 and 1080 nm and they are related to transitions to higher-lying sub-levels of the lower manifold ($^2F_{7/2}$).

The luminescence decay curves of ZnO:Yb ceramics fabricated at 1180 °C and containing 1.0 and 2 wt% Yb are shown in Fig. 13(b). They are clearly not single exponential, so that the mean luminescence lifetime $<\tau_{lum}>$ was calculated. It was 8.7 μs for the 1 wt% Yb doped ceramic and 15.6 μs for the 2 wt% Yb doped one. The radiative lifetime of Yb^{3+} ions in Y_2O_3 τ_{rad} is 0.89 ms [80]. With increasing the Yb doping level up to 100 at% (Yb_2O_3, the stoichiometric composition), the luminescence lifetime is expected to be notably shortened owing to the strong energy transfer to defects and impurities. Indeed, in [81] for bulk Yb_2O_3 crystals, τ_{lum} was determined to be only 15 μs in agreement with our data. The dependence of $<\tau_{lum}>$ on the Yb content in the ceramic can be due to the different content of defects and different size of Yb_2O_3 crystals.

LT (10 K) absorption and luminescence spectra of Yb^{3+} ions were also measured, as shown in Fig. 14(a,b). It is known that in cubic sesquioxides, there are two sites for rare-earth ions having the symmetries of C_2 (3/4 ions) and C_{3i} (1/4 ions) [82]. For the latter sites, the electric dipole transitions of rare-earth ions are forbidden due to the inversion symmetry, so that the spectroscopic properties of cubic sesquioxides are mainly determined by ions residing in the C_2 sites. For these sites, each $^{2S+1}L_J$ multiplet is split into J + 1/2 Stark sub-levels, which are numbered as 0...3 for the ground-state ($^2F_{7/2}$) and 0'...2' for the excited-state ($^2F_{5/2}$). Following [81], an assignment of electronic transitions of Yb^{3+} ions in C_2 sites in Yb_2O_3 crystals in the studied ceramics was performed, Fig. 14(a,b). As a result, we constructed the scheme of energy-levels corresponding to the following experimental crystal-field splitting: $^2F_{7/2}$ = (0, 447, 563, 987) cm^{-1} and $^2F_{5/2}$ = (10245, 10522, 11071) cm^{-1}, Fig. 14(c). For comparison, in the same figure, we showed the crystal-field splitting for Yb^{3+} ions in C_2 sites in Y_2O_3 [81]. The stoichiometric compound Yb_2O_3 provides larger total Stark splitting for Yb^{3+} ions.

The careful examination of the LT absorption and luminescence spectra provided the evidence of Yb^{3+} ions in C_{3i} sites. A close look at the ZPL in absorption, see the inset in Fig. 13(a), indicates a weak side peak at 10256 cm^{-1} (975.0 nm). The excitation into this peak leads to a quite different LT luminescence spectrum, Fig. 14(b). These spectral features are similar to those for bulk Yb:Y_2O_3 crystals [81].

Optical spectroscopy does not reveal any signs of optically active Yb^{3+} ions present in other sites except of those associated with the cubic sesquioxide phase (Yb_2O_3). Such sites may be associated with a small fraction of ytterbium ions adsorbed at the surface of the ZnO grains.

Our studies suggest that ytterbium from this fraction is probably not present in the trivalent state.

3.2.3 X-ray-induced luminescence (spectra and kinetics)

X-ray-induced luminescence (XRIL) spectra of undoped and Yb-doped ZnO ceramics are presented in Fig. 15(a,b). They exhibit two emission bands, namely a short-wavelength band located near the absorption edge of ZnO and having an excitonic nature [83,84], and a broad long-wavelength band which has a defect nature. These two emissions are usually called near-band emission (NBE) and deep band emission (DBE), or green luminescence (GL), respectively. The maximum of the relatively narrow NBE band with smaller intensity is found at 388 nm, and the maximum of the broader and more intense long-wavelength DBE emission band is at 515 nm.

The ZnO emission in the visible spectral range (green, orange, red) is due to the trap states in ZnO [85] and is usually assigned to intrinsic defects [86-90]. The nature of this emission is the subject of many studies. In [86], it was related to zinc vacancies V_{Zn} and oxygen vacancies V_O. In [87,88], a variation of green emissions was ascribed to changes in the charge state of oxygen vacancies with formation of V_O^+ and V_O^{++} centers, while in [89], it was assigned to defects residing on the surface and in the volume of ZnO.

The addition of Yb to the ZnO ceramic leads to a change in the position of the defect emission band in the XRIL spectrum and to a pronounced decrease of its intensity (compare the emission intensities in Fig. 15(a) and Fig. 15(b)). With the addition of 0.2 wt% Yb, the position of the maximum of the DBE band experiences a red shift by ~40 nm and its intensity becomes three times smaller than that for the undoped sample. When increasing the Yb concentration above 0.2 wt%, the intensity of the DBE band is further decreased while its position remains nearly unchanged. The position of the maximum of the DBE band shifts toward shorter wavelengths of 516-519 nm for ceramics fabricated using Yb_2O_3 from the batch No. 2 irrespective of their HPing temperature. Note that the position of the maximum of the DBE band is the same as in the XRIL spectrum of the undoped ZnO ceramic.

The NBE intensity for all ZnO:Yb ceramics is higher than that for the ZnO sample. The highest intensity of the exciton NBE band is observed for the ZnO:2 wt% Yb ceramic.

The decay kinetics of XRIL of ZnO:Yb ceramics are shown in Fig. 16. They were measured without a monochromator, i.e., by detecting the whole XRIL spectrum. The addition of ytterbium ions causes a noticeable change in the shape of the decay curves and makes the decay faster. The decay curves for both undoped and doped ZnO usually have a complex non-exponential shape, which is especially clear for the GL [17]. To have a quantitative estimate of their temporal characteristics, the decay curves were divided into two time domains, the “fast” one from 0 to 75 ns and the “slow” one from 75 to 200 ns. Within these domains, the characteristic decay times were determined using a single-exponential fit. This assessment allows for a technical comparison of the XRIL properties of ceramics with different Yb contents. For the undoped ZnO ceramic, the XRIL decay times within the “fast” and “slow” time domains are τ_{fast} = 38 ns and τ_{slow} = 99 ns, respectively. According to the XRIL spectrum of the undoped ZnO ceramic showing the dominant GL band Fig. 15(a), the characteristic time

τ_{slow} = 99 ns can be assigned to the green defect emission. For the ZnO:Yb ceramics, the XRIL decay curves behave differently in the "fast" and the "slow" time domains, see Table 4. The relative contribution of the "fast" component gradually increases with the Yb content and the τ_{fast} is shortened from 38 ns for the undoped ZnO ceramic to 1.5-3.5 ns for nearly all the Yb-doped ones, making the decay faster. This agrees with the redistribution of intensity of the NBE and DBE bands in the corresponding XRIL spectra, see Fig. 15(a,b), namely, with the increase of the relative intensity of the former band. Thus, the "fast" decay component is assigned to the near-band emission. The ZnO:1 wt% Yb and ZnO:2 wt% Yb ceramics fabricated at 1180 °C using Yb_2O_3 from the batch No. 2 demonstrate the fastest XRIL decay. For the latter ceramic, τ_{fast} = 3.5 ns and τ_{slow} = 52 ns. Thus, Yb doping also affects the "slow" decay time constant. This agrees with the observed variation of the peak position of the DBE band.

We compared the XRIL decay characteristics of three ZnO:Yb ceramics with the same Yb concentration of 1.0 wt% sintered using two different batches of Yb_2O_3 and two different HPing temperatures, 1150 and 1180 °C, see Table 4. The decay curves for these ceramics behave differently in both the "fast" and "slow" domains. The "slow" domain is much more affected by the quality of the initial oxide, which is the reason why the ZnO ceramic fabricated at 1150 °C using Yb_2O_3 from the batch No. 1 has a higher relative intensity of the slow component and the slowest decay time (τ_{fast} = 1.9 ns and τ_{slow} = 53 ns). The ZnO ceramic fabricated at 1150 °C using Yb_2O_3 from the batch No. 2 shows different decay times, τ_{fast} = 5.7 ns and τ_{slow} = 34 ns). Increasing the sintering temperature to 1180 °C results in further variation of the decay times, τ_{fast} = 3.5 ns and τ_{slow} = 45 ns, without a significant change of their relative contributions.

To summarize, introduction of ytterbium gives a rise to a fast decay component with a characteristic decay time τ_{fast} = 1.5-5.7 ns. The tendency in which this decay time changes with increasing ytterbium content is not clear. In the "slow" time domain the registered decay time experiences a non-monotonic decrease with increasing the ytterbium content. The great effect of ytterbium is a decrease in the relative intensity of the slow luminescent component, which makes the decay faster.

The initial concentration of Yb_2O_3, the HPing temperature and uncontrollable impurities in the Yb_2O_3 reagent greatly affect the luminescence decay. In the future, we plan to measure the decay curves in a larger time scale (μs-range).

In this work, we demonstrate a pronounced influence of the Yb addition and increasing its concentration on the properties of the ZnO optical ceramics, into structure of which Yb ions do not enter. Instead, two-phase materials, namely ZnO – Yb_2O_3 composite optical ceramics are formed. Shestakov *et al.* [25] have found that incorporation of ytterbium ions within ZnO crystal lattice is not required for the efficient energy transfer from ZnO to Yb^{3+}. The authors of [25] underline that the nanoscale of the particle size is a principal aspect as it ensures a tight contact between tiny nanosized Yb_2O_3 particles that are attached to larger ZnO nanocrystals and the ZnO nanophase. The nanocomposite is formed, and the energy transfer takes place between zinc oxide nanocrystals and ytterbium oxide nanoparticles on their surface. Recently, the formation of an Yb_2O_3-ZnO heterojunction was proposed by Cerrato *et al.* [30,31]. They suggested a hypothetical working mechanism of a hole transfer from ZnO valence band to

Yb_2O_3 valence band, improving charge carrier separation. It is interesting that a tight contact between microcrystals of Yb_2O_3 and larger ZnO crystals in optical ceramics also ensures an effective interaction on the interface of these crystals which results in modification of the spectral-luminescent properties of these ZnO – Yb_2O_3 composite optical ceramics.

4. Conclusions

We report on the fabrication, structure, morphology and optical and X-ray spectroscopy of undoped and Yb-doped hexagonal zinc oxide optical ceramics. A comprehensive study of the effect of Yb concentration in the range of 0.2 - 2.0 wt% and hot pressing temperature (1150 and 1180 °C) on the properties of ceramics was performed. It was found that Yb^{3+} ions do not enter the structure of ZnO crystals but are located at the grain surfaces and form cubic crystals of Yb_2O_3. The doping with 0.2 – 0.4 wt% Yb leads to a decrease in the grain size of ZnO ceramics from 23 to 4 μm, while further increase in the ytterbium content to 1.0 wt% has practically no effect on the grain size of ZnO crystals. This dependence relates to crystallization of additional crystalline phase of ytterbium sesquioxide (ytterbia), which influences the growth rates of certain ZnO faces. A decrease in the grain size of ZnO ceramics increases the number of contact interactions at the interfaces of ZnO and Yb_2O_3 crystals.

The studies of transmittance spectra of ceramics demonstrate the possibility of developing ZnO:Yb ceramics with a transmittance of 40-60% in the visible spectral range. The increase of Yb concentration leads to a shift toward shorter wavelengths of the long-wavelength transparency edge of ceramics by 1.5–2 μm as compared to undoped samples, which is caused by an increase in the concentration of free charge carriers. An increase in the hot pressing temperature of Yb-doped ceramics causes a decrease in the concentration of free charge carriers.

The absorption spectra of ZnO:Yb ceramics contain an absorption band of Yb^{3+} ions which greatly resembles that for bulk Yb^{3+}-doped sesquioxide crystals, e.g., Yb^{3+}:Y_2O_3 and Yb_2O_3. The applicability of the Beer's law indicates a constant distribution of ions between the surface of the ZnO crystals and the ytterbium sesquioxide crystals. An increase in the hot pressings temperature from 1150 to 1180 °C leads to a redistribution of Yb^{3+} ions between the grain boundaries of ZnO and Yb_2O_3 crystals.

The studies of X-ray induced luminescence spectra have shown that doping of ZnO ceramic with Yb leads to a significant suppression of the intensity of the long-wavelength (515-540 nm) emission band of ZnO, which has a defect nature and to a certain increase in the near-edge exciton band with a maximum at about 389 nm. It also gives rise to a fast decay component with a characteristic decay time τ_{fast} = 1.5-5.7 ns. The “slow” decay time constant in the range of 75-200 ns assigned to defect emission decreases non-monotonically from 96 to 34 ns with an increase in the Yb concentration. Bearing in mind high adhesion at the ZnO and Yb_2O_3 oxide interfaces, we can assume the leading role of the special (nonequilibrium) state of the electronic structure of the grain boundaries in the processes of interaction and transfer of excitation energy from between the ZnO crystals and Yb^{3+} ions, which leads to an increase in the near-band-edge emission intensity.

The obtained results indicate that the developed ZnO: Yb optical ceramics are promising as scintillating materials. Once optimized for Yb concentration, the hot-pressing temperature, as well as potential additional heat-treatments, they can become new materials for the rapid development of scintillators.

Acknowledgements

This work was partly supported by the RFBR (Grant 19-03-00855).

References

1. U. Orgur, Ya.I. Alivov, C. Liu, A. Teke, M.A. Reshnikov, S. Dogan, V. Avrutin, S.-J. Cho, H. Morkoc, A comprehensive review of ZnO materials and devices, J. Appl. Phys. 98 (2005) 041301-1-103, https://doi.org/10.1063/1.1992666.

2. C. Klingshirn, J. Fallert, H. Zhou, J. Sartor, C. Thiele, F. Maier-Flaig, D. Schneider, H. Kalt, 65 years of ZnO research – old and very recent results, Phys. Status Solidi B. 247 (2010) 1424–1447, https://doi.org/10.1002/pssb.200983195.

3. P.A. Rodnyi, I.V. Khodyuk, Optical and luminescence properties of zinc oxide, Opt. Spectrosc. 111 (2011) 776-785, https://doi.org/10.1134/S0030400X11120216.

4. R. John, R. Rajakumari, Synthesis and characterization of rare earth ion doped nano ZnO, Nano-Micro Lett. 4 (2012) 65−72, http://dx.doi.org/10.3786/nml.v4i2.p65-72.

5. V. Kumar, O.M. Ntwaeaborwa, T. Soga, V. Dutta, H.C. Swart, Rare earth doped zinc oxide nanophosphor powder: A future material for solid state lighting and solar cells, ACS Photonics 4 (2017) 2613-2637, https://doi.org/10.1021/acsphotonics.7b00777.

6. J.S. Neal, D.M. DeVito, B.L. Armstrong, M. Hong, B. Kesanli, X. Yang, N.C. Giles, J.Y.Howe, J.O. Ramey, D.J. Wisniewski, M. Wisniewska, Z.A. Munir, L.A. Boatner, Investigation of ZnO-based polycrystalline ceramic scintillators for use as α-particle detectors, IEEE Trans. Nucl. Sci. 56 (2009) 892-898, https://doi.org/10.1109/TNS.2008.2004702.

7. E.I. Gorokhova, P.A. Rodnyi, E.P. Lokshin, K.P. Lott, G.B. Kunshina, K.A. Chernenko, G.V. Ananieva, S.B. Eron'ko, I.V. Khodyuk, O.G. Gromov, E.A. Oreschenko, Structural, optical, and scintillation characteristics of ZnO ceramics, J. Opt. Technol. 78 (2011) 753-760, https://doi.org/10.1364/JOT.78.000753.

8. M. Prakasamn, O. Viraphong, D. Michau, A. Largeteau, Critical parameters to obtain Yb^{3+} doped Lu_2O_3 and ZnO transparent ceramics, Ceram. Intern. 40 (2014) 1859–1864, http://dx.doi.org/10.1016/j.ceramint.2013.07.088.

9. M. Hohg, D. Fredrick, X. Yang, J.S. Neal, Z.A. Munir, Characterization of green-emitting translucent zinc oxide ceramics prepared via spark plasma sintering, Int. J. Appl. Ceram. Technol. 8 (2011) 725–733, http://dx.doi.org/10.1111/j.1744-7402.2010.02527.x.

10. E.I. Gorokhova, G.V. Anan'eva, V.A. Demidenko, P.A. Rodnyi, I.V. Khodyuk, E.D. Bourret-Courchesne, Optical, luminescence, and scintillation properties of ZnO and ZnO:Ga ceramics, J. Opt. Technol. 75 (2008) 741–746, https://doi.org/10.1364/JOT.75.000741.

11. V.A. Demidenko, E.I. Gorokhova, I.V. Khodyuk, O.A. Khristich, S.B. Mikhrin, P.A. Rodnyi, Scintillation properties of ceramics based on zinc oxide, Radiat. Meas. 42 (2007) 549-552, https://doi.org/10.1016/j.radmeas.2007.01.050.
12. P.A. Rodny, I.V. Khodyuk, E.I. Gorokhova, S.B. Mikhrin, P. Dorenbos, Emission and excitation spectra of ZnO:Ga and ZnO:Ga,N ceramics, Opt. Spectrosc. 105 (2008) 908-912, https://doi.org/10.1134/S0030400X08120151.
13. E.I. Gorokhova, S.B. Eron'ko, E.A. Oreshchenko, A.V. Sandulenko, P.A. Rodnyi, K.A. Chernenko, I.D. Venevtsev, A.M. Kul'kov, F. Muktepavela, P. Boutachkov, Structural, optical, and luminescence properties of ZnO:Ga optical scintillation ceramic, J. Opt. Technol. 85 (2018) 729-737, https://doi.org/10.1364/JOT.85.000729.
14. K.A. Chernenko, E.I. Gorokhova, S.B. Eron'ko, A.V. Sandulenko, I.D. Venevtsev, H. Wieczorek, P.A. Rodnyi, "Structural, optical and luminescent properties of ZnO:Ga and ZnO:In ceramics, IEEE Trans. Nucl. Sci. 65 (2018) 2196–2202, https://doi.org/10.1109/TNS.2018.2810331.
15. I.D. Venevtsev, A.P. Tarasov, A.E. Muslimov, E.I. Gorokhova, L.A. Zadorozhnaya, P.A. Rodnyi, V.M. Kanevsky, Ultraviolet luminescence of ZnO whiskers, nanowalls, multipods, and ceramics as potential materials for fast scintillators, Materials 14 (2021) 2001-1-13, https://doi.org/10.3390/ma14082001.
16. F. Muktepavela, A. Zolotarjovs, R. Zabels, K. Kundzins, E. Gorokhova, E. Tamanis, Comparative study on micromechanical properties of ZnO:Ga and ZnO:In luminescent ceramics, Latv. J. Phys. Tech. Sci., 58 (202) 23-32, https://doi.org/10.2478/lpts-2021-0003.
17 6. E.I. Gorokhova, S.B. Eron'ko, A.M. Kul'kov, E.A. Oreshchenko, K.L. Simonova, K.A. Chernenko, I.D. Venevtsev, P.A. Rodnyĭ, K.P. Lott, H. Wieczorek, Development and study of ZnO:In optical scintillation ceramic, J. Opt. Techol. 82 (2015) 837–842, https://doi.org/10.1364/JOT.82.000837.
18 7. E.I. Gorokhova, S.B. Eron'ko, E.A. Oreshchenko, P.A. Rodnyi, I.D. Venevtsev, A.M. Kul'kov, E.S. Sukharzhevskaya, Structural, optical, and luminescence properties of ZnO:Er ceramic, J. Opt. Technol. 86 (2019) 814-819, https://doi.org/10.1364/JOT.86.000814.
19 8. E. Gorohova, L. Basyrova, I. Venevtsev, I. Alekseeva, A. Khubetsov, O. Dymshits, M. Baranov, M. Tsenter, A. Zhilin, S. Eron'ko, E. Oreschenko, P. Rodnyi, P. Loiko, Structure and spectral-luminescent properties of Er^{3+}:ZnO optical ceramics, J. Phys. Conf. Ser. 1965 (2020) 012041-1-6, https://iopscience.iop.org/article/10.1088/1742-6596/1695/1/012041.
20 19. L. Laversenne, Y. Guyot, C. Goutaudier, M. T. Cohen-Adad, G. Boulon, Optimization of spectroscopic properties of Yb^{3+}-doped refractory sesquioxides: Cubic Y_2O_3, Lu_2O_3 and monoclinic Gd_2O_3, Opt. Mater. 16, 475–483 (2001), https://doi.org/10.1016/S0925-3467(00)00095-1.
21 0. J. Sowik, M. Miodyńska, B. Bajorowicz, A. Mikołajczyk, W. Lisowski, T. limczuk, D. Kaczor, A. Zaleska Medynska, A. Malankowska, Optical and photocatalytic properties of rare earth metal-modified ZnO quantum dots, Appl. Surf. Sci. 464 (2019) 651-663, https://doi.org/10.1016/j.apsusc.2018.09.104.

22 1. U. Pal, R. Meléndrez, V. Chernov, and M. Barboza-Flores, Thermoluminescence properties of ZnO and ZnO:Yb nanophosphors, Appl. Phys. Lett. 89 (2006) 183118-1-3, https://doi.org/10.1063/1.2374866.
23 2. M. Shestakov, A. Baranov, V. Tikhomirov, Y. Zubavichus, A. Kuznetsov, A. Veligzhanin, A. Kharin, R. Rösslhuber, V. Timoshenko, V, Moshchalkov, Energy-transfer luminescence of a zinc oxide/ytterbium oxide nanocomposite, RSC Adv. 2 (2012) 8783-8788, https://doi.org/10.1039/C2RA20755A.
24 3. G.L. Kabongo, G.H. Mhlongo, B.M. Mothudi, K.T. Hillie, H.C. Swart, M.S. Dhlamini, Enhanced exciton emission from ZnO nano-phosphor induced by Yb^{3+} ions, Mater. Lett. 119 (2014) 71-74, http://dx.doi.org/10.1016/j.matlet.2013.12.076.
25 4. R. Zamiri, A.F. Lemos, A. Reblo, H.A. Ahangar, J.M.F. Ferreira, Effects of rare-earth (Er, La and Yb) doping on morphology and structure properties of ZnO nanostructures prepared by wet chemical method, Ceram. Int. 40 (2014) 523-529, http://dx.doi.org/10.1016/j.ceramint.2013.06.034.
26 5. O.A. Shalygina, I.V. Nazarov, A.V. Baranov, V. Yu. Timoshenko, Structure and photoluminescence properties of zinc oxide/ytterbium oxide nanocomposites. J. Sol-Gel Sci. Technol. 81 (2017) 333–337, https://doi.org/10.1007/s10971-016-4258-y.
27. M.M. Rahman, M.M. Alam, A.M. Asiri, M.R. Awual, Fabrication of 4-aminophenol sensor based on hydrothermally prepared ZnO/Yb_2O_3 nanosheets, New J. Chem. 41 (2017) 9159–9169, https://doi.org/10.1039/c7nj01623a.
28. E. Cerrato, C. Gionco, I. Berruti, F. Sordello, P. Calza, M.C. Paganini, Rare earth ions doped ZnO: Synthesis, characterization and preliminary photoactivity assessment, J. Solid State Chem. 264 (2018) 42–47, https://doi.org/10.1016/j.jssc.2018.05.001.
29. F. Sordello, I. Berruti, C. Gionco, M.C. Paganini, P. Calza, C. Minero, Photocatalytic performances of rare earth element-doped zinc oxide toward pollutant abatement in water and wastewater, Appl. Catal. B 245 (2019) 159-166, https://doi.org/10.1016/j.apcatb.2018.12.053.
30. E. Cerrato, G.A. Zickler, M.C. Paganini, The role of Yb doped ZnO in the charge transfer process and stabilization, J. Alloy. Compd. 816 (2020) 152555-1-7, https://doi.org/10.1016/j.jallcom.2019.152555.
31. E. Cerrato, N.P.F. Gonçalves, P. Calza, M.C. Paganini, Comparison of the photocatalytic activity of ZnO/CeO_2 and ZnO/Yb_2O_3 mixed systems in the phenol removal from water: A mechanicistic approach, Catalysts 10 (2020) 1222-1-15, https://doi.org/10.3390/catal10101222.
32. I. Soumahoro, G. Schmerber, A. Douayar, S. Colis, M. Abd-Lefdil, N. Hassanain, A. Berrada, D. Muller, A. Slaoui, H. Rinnert, A. Dinia, Structural, optical and electrical properties of Yb doped ZnO thin films prepared by spray pyrolysis method. J. Appl. Phys. 109 (2011) 033708, https://doi.org/10.1063/1.3544307.
33. M. Balestrieri, G. Ferblantier, S. Colis, G. Schmerber, C. Ulhaq-Bouillet, D. Muller, A. Slaoui, A. Dinia, Structural and optical properties of Yb-doped ZnO films deposited by magnetron reactive sputtering for photonconversion, Sol. Energy Mater. Sol. Cells 117 (2013) 363-371, http://dx.doi.org/10.1016/j.solmat.2013.06.032.

34. R. Okada, W. Miao, Y. Terai, T. Tsuji, Y. Fujiwara, Sputtering-assisted metal-organic chemical vapor deposition of Yb-doped ZnO for photonic conversion in Si solar cells, Phys. Status Solidi C 11 (2014) 1292–1295, https://doi.org/10.1002/pssc.201300614.
35. C.L. Heng, T. Wang, W.Y. Su, H.C. Wu, M.C. Yang, L.G. Deng, P.G. Yin, T.G. Finstad, Intense ultraviolet photoluminescent emission from Yb doped ZnO thin films on Si after high temperature annealing, J. Alloy. Compd. 695 (2017) 2232-2237, https://doi.org/10.1016/j.jallcom.2016.11.072.
36. E. Guziewicz, R. Ratajczak, M. Stachowicz, D. Snigurenko, T.A. Krajewski, C. Mieszczynski, K. Mazur, B.S. Witkowski, P. Dluzewski, K. Morawiec, A. Turos, Atomic layer deposited ZnO films implanted with Yb: The influence of Yb location on optical and electrical properties, Thin Solid Films 643 (2017) 7-15, https://doi.org/10.1016/j.tsf.2017.08.014.
37. I.N. Demchenko, Y. Melikhov, P. Konstantynov, R. Ratajczak, A. Barcz, E. Guziewicz, Resonant photoemission spectroscopy study on the contribution of the Yb 4f states to the electronic structure of ZnO, Acta Phisica Polonica A 133 (2018) 907-909, https://doi.org/10.12693/APhysPolA.133.907.
38. I.N. Demchenko, R. Ratajczak, Y. Melikhov, P. Konstantynov, E. Guziewicz, Valence band of ZnO:Yb probed by resonant photoemission spectroscopy, Mater. Sci. Semicond. Process. 91 (2019) 306–309, https://doi.org/10.1016/j.mssp.2018.11.037.
39. C. Guillaume, C. Labbé, C. Frilay, J. Doualan, F. Lemarié, L. Khomenkova, L. Borkovska, X. Portier, Thermal treatments and photoluminescence properties of ZnO and ZnO:Yb films grown by magnetron sputtering, Phys. Status Solidi 216 (2019) 1800203, http://dx.doi.org/10.1002/pssa.201800203.
40. E. Guziewicz, S. Kobyakov, R. Ratajczak, A. Wierzbicka, W. Wozniak A. Kaminska, Optical response of epitaxial ZnO films grown by atomic layer deposition and coimplanted with Dy and Yb, Phys. Status Solidi B (2020) 1900513-1-7, https://doi.org/10.1002/pssb.201900513.
41. C.L. Heng, C.N. Zhao, L. Zhang, W. Xiang, W.Y. Su, H.X. Yin, Y.K. Gao, P.G. Yin, T.G. Finstad, Effects of Yb doping on the structure and near band-edge emission of ZnO thin films on Si after high temperature annealing, J. Lumin. 222 (2020) 117153, https://doi.org/10.1016/j.jlumin.2020.117153.
42. H.T. Kim, S.-Y. Lee, A. Slaoui, A. Dinia, H.J. Jeon, C. Park, Properties of Yb-added ZnO (Yb:ZnO) films as an energy-conversion layer on polycrystalline silicon solar cells, Mat. Chem. Phys. 265 (2021) 124513-1-5, https://doi.org/10.1016/j.matchemphys.2021.124513.
43. E.R. López-Mena, O. Ceballos-Sanchez, T.J.N. Hooper, G. Sanchez-Ante, M. Rodríguez-Muñoz, J.A. Renteria-Salcedo, A. Elías-Zuñiga, A. Sanchez-Martinez, The effect of Yb doping on ZnO thin films obtained via a low-temperature spin coating method, J. Mater. Sci.: Mater. Electron. 32 (2021) 347–359, https://doi.org/10.1007/s10854-020-04785-7.
44. R. Khanum, R.S. Moirangthem, N.M. Das, Observation of defect-assisted enhanced visible whispering gallery modes in ytterbium-doped ZnO microsphere, J. Appl. Phys 121 (2017) 213101-1-6, https://doi.org/10.1063/1.4984205.

45. R. Ratajczak, S. Prucnal, E. Guziewicz, C. Mieszczynski, D. Snigurenko, M. Stachowicz, W. Skorupa, and A. Turos, The photoluminescence response to structural changes of Yb implanted ZnO crystals subjected to non-equilibrium processing, J. Appl. Phys. 121 (2017) 075101-1-9, http://aip.scitation.org/toc/jap/121/7.
46. R. Ratajczak, C. Mieszczynski, S. Prucnal, T.A. Krajewski, E. Guziewicz, W. Wozniak, K. Kopalko, R.Heller, S. Akhmadaliev, Correlations between the structural transformations and concentration quenching effect for RE-implanted ZnO systems, Appl. Surf. Sci. 521 (2020) 146421-1-8, https://doi.org/10.1016/j.apsusc.2020.146421.
47. E. Cerrato, C. Gionco, M.C. Paganini, E. Giamello, E. Albanese, G. Pacchioni, Origin of visible light photoactivity of the CeO_2/ZnO heterojunction, ACS Appl. Energy Mater. 1 (2018) 4247-4260, https://doi.org/10.1021/acsaem.8b00887.
48. S. Bachir, K. Azuma, J. Kossanyi, P. Valat, and J. C. Ronfard-Haret, Photoluminescence of polycrystalline zinc oxide co-activated with trivalent rare-earth ions into zinc oxide, J. Lumin. 75 (1997) 35–49, https://doi.org/10.1016/S0022-2313(97)00093-8.
49. Y.F. Bai, Y.X. Wang, K. Yang, X.R. Zhang, Y.L. Song, C.H. Wang, Enhanced up converted photoluminescence in Er^{3+} and Yb^{3+} codoped ZnO nanocrystals with and without Li^+ ions, Opt. Commun. 281 (2008) 5448–5452, https://doi.org/10.1016/j.optcom.2008.07.041.
50. S. Ye, N. Jiang, F. He, X. Liu, B. Zhu, Y. Teng, J.R. Qiu, Intense near-infrared emission from ZnO-$LiYbO_2$ hybrid phosphors through efficient energy transfer from ZnO to Yb^{3+}, Opt. Express 18 (2010) 639-644, https://doi.org/10.1364/OE.18.000639.
51. A. Balakrishna, T.K. Pathak, E. Coetsee-Hugo, V. Kumar, R.E. Kroon, O.M. Ntwaeaborwa, H.C. Swart, Synthesis, structure and optical studies of ZnO:Eu^{3+}, Er^{3+}, Yb^{3+} thin films: enhanced up-conversion emission, Colloid. Surf. Physicochem. Eng. Asp. 540 (2018) 123-135, https://doi.org/10.1016/j.colsurfa.2017.12.066.
52. T. Munawar, S. Yasmeen, M. Hasan, K. Mahmood, A. Hussain, A. Ali, M.I. Arshad, F. Iqbal, Novel tri-phase heterostructured ZnO–Yb_2O_3–Pr_2O_3 nanocomposite; structural, optical, photocatalytic and antibacterial studies, Ceram. Intern. 46 A (2020) 11101-11114, https://doi.org/10.1016/j.ceramint.2020.01.130.
53. K. Raju, V. Prasad, Effect of capacitance on ZnO-Bi_2O_3-Yb_2O_3 based varistor for nanosecond transients, J. Central South University 25 (2018) 2332-2338, https://doi.org/10.1007/s11771-018-3917-2.
54. J.L. He, J. Hu, Y.H. Lin, ZnO varistors with high voltage gradient and low leakage current by doping rare-earth oxide, Sci. China Ser. E-Tech Sci. 51 (2008) 693-701, https://doi.org/10.1007/s11431-008-0085-x.
55. MAUD materials analysis using diffraction, a Rietveld extended program to perform the combined analysis, http://maud.radiographema.eu/
56. J.A.R. Márquez, C.M.B. Rodríguez, C.M. Herrera, E.R. Rosas, O.Z. Angel, O.T. Pozos, Effect of surface morphology of ZnO electrodeposited on photocatalytic oxidation of methylene blue dye. Part I: Analytical study, Int. J. Electrochem. Sci. 6 (2011) 4059–4069.
57. C.A. Arguello, D.L. Rousseau, S.P.S. Porto, First-order Raman effect in wurtzite-type crystals, Phys. Rev. 181 (1969) 1351-1363, https://doi.org/10.1103/PhysRev.181.1351.

58. R. Cusco, E. Alarcon-Llado, J. Ibanez, L. Artus, J. Jimenez, B. Wang, M. J. Callahan, Temperature dependence of Raman scattering in ZnO, Phys. Rev. B 75 (2007) 165202-1-11, https://doi.org/10.1103/PhysRevB.75.165202.
59. T.C. Damen, S.P.S. Porto, B. Tell, Raman effect in zinc oxide, Phys. Rev. 142 (1966) 570-574, https://doi.org/10.1103/PhysRev.142.570.
60. J.M. Calleja, M. Cardona, Resonant Raman scattering in ZnO, Phys. Rev. B 16 (1977) 3753-3761, https://doi.org/10.1103/PhysRevB.16.3753.
61. J. Yu, L. Cui, H. He, S. Yan, Y. Hu, H. Wu, Raman spectra of RE_2O_3 (RE=Eu, Gd, Dy, Ho, Er, Tm, Yb, Lu, Sc and Y): laser-excited luminescence and trace impurity analysis, J. Rare Earth 32 (2014) 1-4, https://doi.org/10.1016/S1002-0721(14)60025-9.
62. S.D. Pandey, K. Samanta, J. Singh, N.D. Sharma, A.K. Bandyopadhyay, Anharmonic behavior and structural phase transition in Yb_2O_3, AIP Adv. 3 (2013) 122123-1-11 https://doi.org/10.1063/1.4858421.
63. G. Schaack, J.A. Koningstein, Phonon and electronic Raman spectra of cubic rare-earth oxides and isomorphous yttrium oxide, J. Opt. Soc. Am. 60 (1970) 1110-1115, https://doi.org/10.1364/JOSA.60.001110.
64. C.K. Gupta, N. Krishnamurthy, Extractive metallurgy of rare earths, CRC Press, 2005, 521 p.
65. L.G. Berry, Brian Mason, R.V. Dietrich, Mineralogy - Concepts, Descriptions, Determinations, W.H. Freeman and Co., San Francisco, 1983, 561 p.
66. E.V. Kortounova , V.I. Lyutin , V.D. Dubovskaya and P.P. Chvanski, The growth of zinc oxide crystals with impurities, High Press Res., 20 (1-6) (2001) 175-183, https://doi.org/10.1080/08957950108206165.
67. L.N. Demianets, D.V. Kostomarov, I.P. Kuz'mina, S.V. Pushko, Mechanism of growth of ZnO single crystals, Crystallogr. Rep. 47 (2002) S86–S98, https://doi.org/10.1134/1.1529962.
68. N.V. Belov, The structure of ionic crystals and of the metallic phases, Moscow, the USSR Academy of Sciences Publishing House, 1947.
69. T.K. Karipidis, V.V. Mal'tsev, E.A. Volkova, M.V. Chukichev, N.I. Leonyuk, Thermal stability of zincite single crystals, Crystallogr. Rep. 53 (2008) 326–330, https://doi.org/10.1134/S1063774508020247.
70. N.P. Yushkin, I.I. Shafranovskii, K.P. Yanulov, Zakony simmetrii v mineralogii (The laws of symmetry in mineralogy), Leningrad: Nauka, 1987, 335 p. [In Russian].
71. E.V. Kortunova, V.I. Lyutin, *Sintez mineralov* (Synthesis of Minerals), Aleksandrov: VNIISIMS, 2000, vol. 1, p. 403.
72. F. Jiang, Z. Peng, Y. Zang, X. Fu, Progress on rare-earth doped ZnO-based varistor materials. J. Adv. Ceram. 2 (2013) 201–212, https://doi.org/10.1007/s40145-013-0071-z.
73. S. Sambasivama, D.P. Joseph, S.A. Naidu, K.N. Hule, K.S. Hui, B.C. Choi, Intense violet–blue emission and paramagnetism of nanocrystalline Gd^{3+} doped ZnO ceramics J. Adv. Ceram. 4 (2015) 300–306, https://doi.org/10.1007/s40145-015-0164-y.

74. C.W. Nahm, Major effects on non-ohmic properties and aging stress behavior of ZPCCD semiconducting varistors with Er_2O_3 doping changes, Trans. Electr. Electron. Mater. 19 (2018) 330–336, https://doi.org/10.1007/s42341-018-0060-6.
75. D.G. Thomas, Infrared absorption in zinc oxide crystals, J. Phys. Chem. Solids 10 (1959) 47-51, https://doi.org/10.1016/0022-3697(59)90124-6.
76. I.P. Kuz′mina, V.A. Nikitenko, Zinc oxide. Production and optical properties. Moscow. Izd. Nauka, 1984. 167 p. [In Russian].
77. N.Y. Garces, L. Wang, N.C. Giles, L.E. Halliburton, Thermal diffusion of lithium acceptors into ZnO crystals. J. Electron. Mater. 32 (2003) 766–771, https://doi.org/10.1007/s11664-003-0068-4.
78. P.Y. Emelie, J.D. Phillips, B. Buller, U.D. Venkateswaran, Free carrier absorption and lattice vibrational modes in bulk ZnO, J. Electron. Mater. 35 (2006) 525–529, https://doi.org/10.1007/s11664-006-0094-0.
79. X.C. Yang, Electrical and optical properties of zinc oxide for scintillator applications, (2008). Graduate Theses, Dissertations, and Problem Reports, 2729, https://researchrepository.wvu.edu/etd/2729, https://doi.org/10.33915/etd.2729.
80. S. Balabanov, D. Permin, T. Evstropova, P. Andreev, L. Basyrova, P. Camy, M. Baranov, X. Mateos, P. Loiko, Hot pressing of Yb:Y_2O_3 laser ceramics with LiF sintering aid, Opt. Mater. 119 (2021) 111349-1-12, https://doi.org/10.1016/j.optmat.2021.111349.
81. V. Peters, Growth and Spectroscopy of Ytterbium-Doped Sesquioxides, Dissertation, Shaker Verlag, Aachen, Germany, 2001.
82. W. Jing, P. Loiko, L. Basyrova, Y. Wang, H. Huang, P. Camy, U. Griebner, V. Petrov, J. M. Serres, M. Aguiló, F. Díaz, X. Mateos, Synthesis, spectroscopy and laser operation of highly-doped “mixed” 10 at.% Yb:$(Lu,Sc)_2O_3$ ceramics, Opt. Mater. 117 (2021) 111128-1-7 https://doi.org/10.1016/j.optmat.2021.111128.
83. B.K. Meyer, H. Alves, D.M. Hofmann, W. Kriegseis, D. Forster, F. Bertram, J. Christen, A. Hoffmann, M. Straßburg, M. Dworzak, U. Haboeck, and A.V. Rodina, Bound exciton and donor–acceptor pair recombinations in ZnO, Phys. Status Solidi B 241 (2004) 231-260, https://doi.org/10.1002/pssb.200301962.
84. A. Teke, U. Ozgur, S. Dogan, X. Gu, H. Morkoc, B. Nemeth, J. Nause, H.O. Everitt, Excitonic fine structure and recombination dynamics in single-crystalline ZnO, Phys. Rev. B 70 (2004) 195207-1-10, https://doi.org/10.1103/PhysRevB.70.195207.
85. D.C. Reynolds, D.C. Look, B. Jogai, Fine structure on the green band in ZnO, J. Appl. Phys. 89 (2001) 6189-6191, https://doi.org/10.1063/1.1356432.
86. T.M.Borseth, B.G. Svensson, A.Yu. Kuznetsov, Identification of oxygen and zinc vacancy optical signals in ZnO, Appl. Phys. Lett. 89 (2006) 262112, https://doi.org/10.1063/1.2424641.
87. C. Ton-That, L. Weston, and M.R. Phillips, Characteristics of point defects in the green luminescence from Zn- and O-rich ZnO, Phys. Rev. B. 86 (2012) 115205, https://doi.org/10.1103/PhysRevB.86.115205.

88. J.D. Ye, S.L. Gu, F. Qin, S.M. Zhu, S.M. Liu, X. Zhou, W. Liu, L.Q. Hu, R. Zhang, Y. Shi, Y.D. Zheng, Correlation between green luminescence and morphology evolution of ZnO films, Appl. Phys. A 81 (2005) 759–762, https://doi.org/10.1007/s00339-004-2996-0.
89. Y.Y. Tay, T.T. Tan, F. Boey, M.H. Liang, J. Ye, Y. Zhao, T. Norby, S. Li, Correlation between the characteristic green emissions and specific defects of ZnO, Phys. Chem. Chem. Phys. 12 (2010) 2373–2379, https://doi.org/10.1039/B922372J.
90. P. Loiko, T. Bora, J.M. Serres, H. Yu, M. Aguiló, F. Díaz, U. Griebner, V. Petrov, X. Mateos, J. Dutta, Oriented zinc oxide nanorods: A novel saturable absorber for lasers in the near-infrared, Beilstein J. Nanotechnol., 9(1) (2018) 2730-2740.

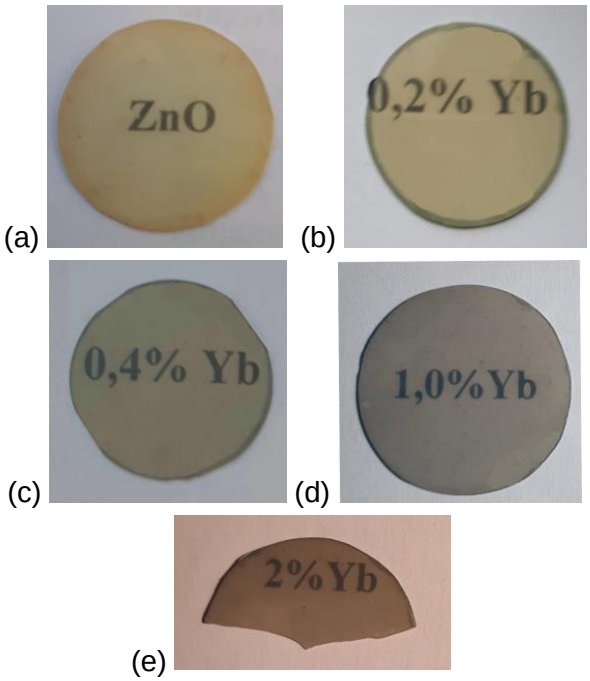

Figure 1. Photographs of (a) undoped and (b-e) Yb^{3+}-doped ZnO transparent ceramics with different Yb doping levels (indicated by labels, in wt%). The ceramics containing 0 – 0.8 wt% Yb were prepared at 1150 °C using Yb_2O_3 from the batch No. 1. The ceramics containing 1 and 2 wt% Yb were prepared at 1180 °C using Yb_2O_3 from the batch No. 2.

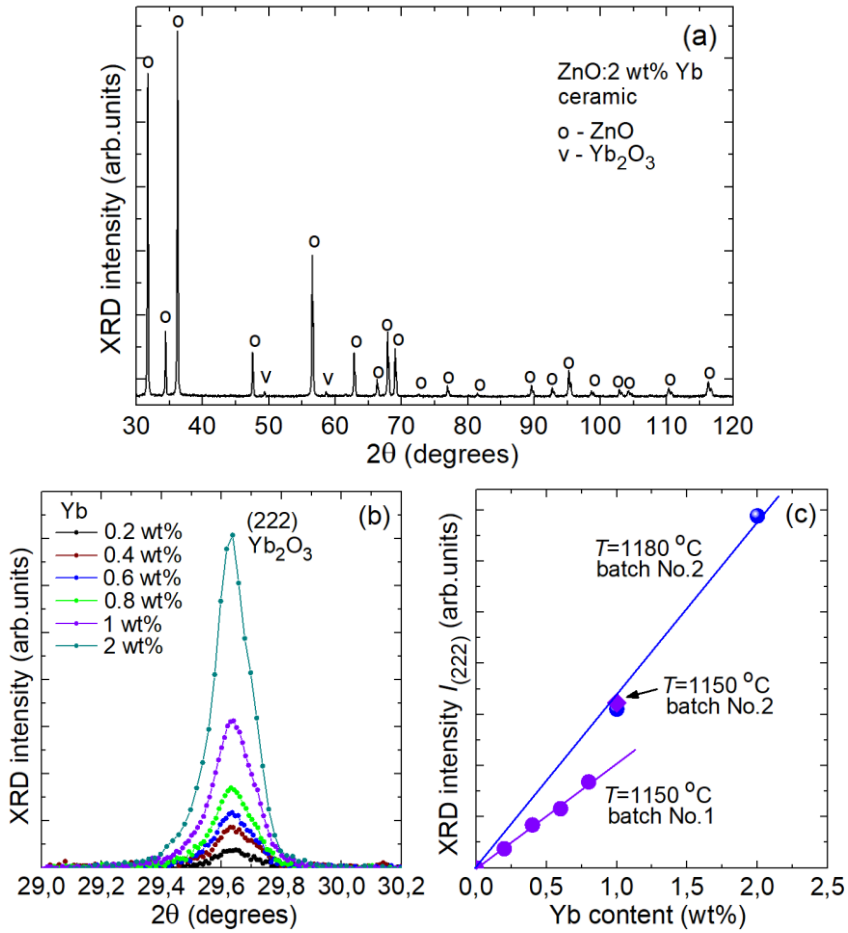

Figure 2. (a) XRD pattern of the ZnO: 2 wt% Yb ceramic; (b) XRD patterns of ZnO:Yb ceramics with different Yb doping level in the 2θ range of 29.0-30.2° corresponding to the (222) peak of Yb_2O_3; the ZnO: 1 wt% Yb ceramic (Yb_2O_3 from the batch No.2) was sintered at 1180 °C; (c) dependence of the corresponding peak diffraction intensity at 2θ ~ 29.63° on the Yb concentration, the synthesis temperatures are 1150 and 1180 °C. The source of Yb_2O_3 is denoted.

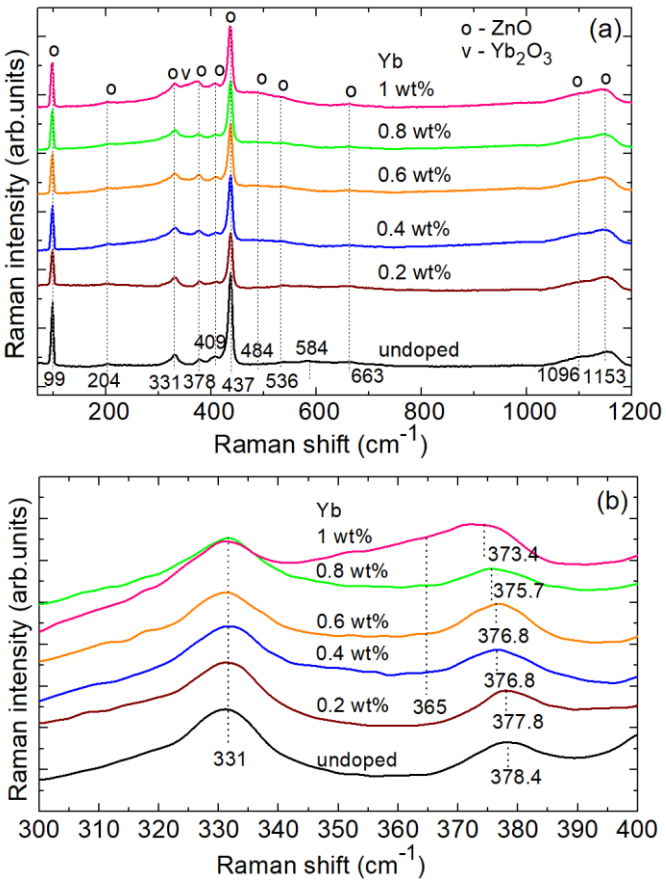

Figure 3. Raman spectra of ZnO optical ceramics, undoped and doped with 0.2 - 1.0 wt% Yb (Yb_2O_3 from batch No. 1): (a) the spectral range 70 - 1200 cm^{-1}; (b) the spectral range 300 - 400 cm^{-1}. The synthesis temperature is 1150 °C. λ_{exc} = 514 nm. *Numbers* indicate the Raman peak frequencies in cm^{-1}. The curves are shifted for the convenience of observation.

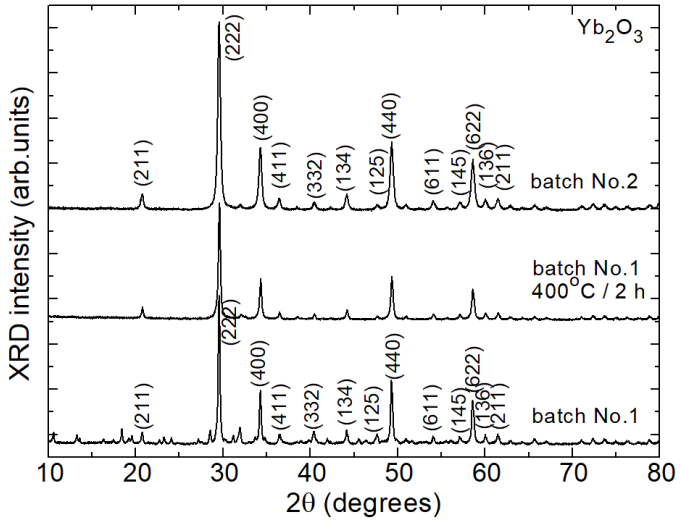

Figure 4. XRD patterns of the Yb_2O_3 reagent from the batch No. 1 (initial and calcined at 400 °C for 2 h) and the batch No. 2 (initial).

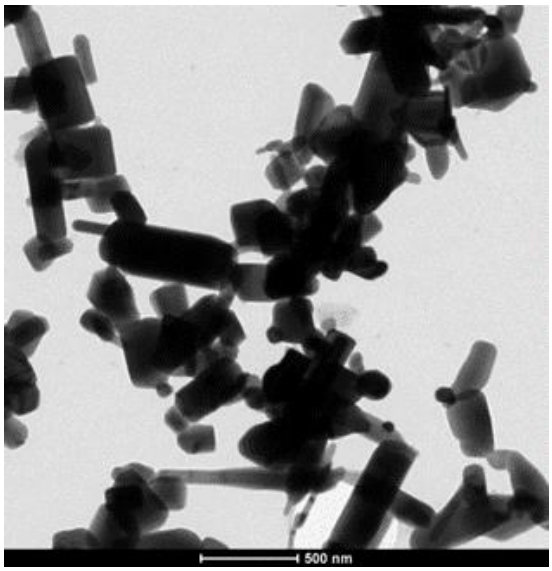

Figure 5. A typical TEM image of the commercial reagent-grade ZnO powder (Zinsa, Peru).

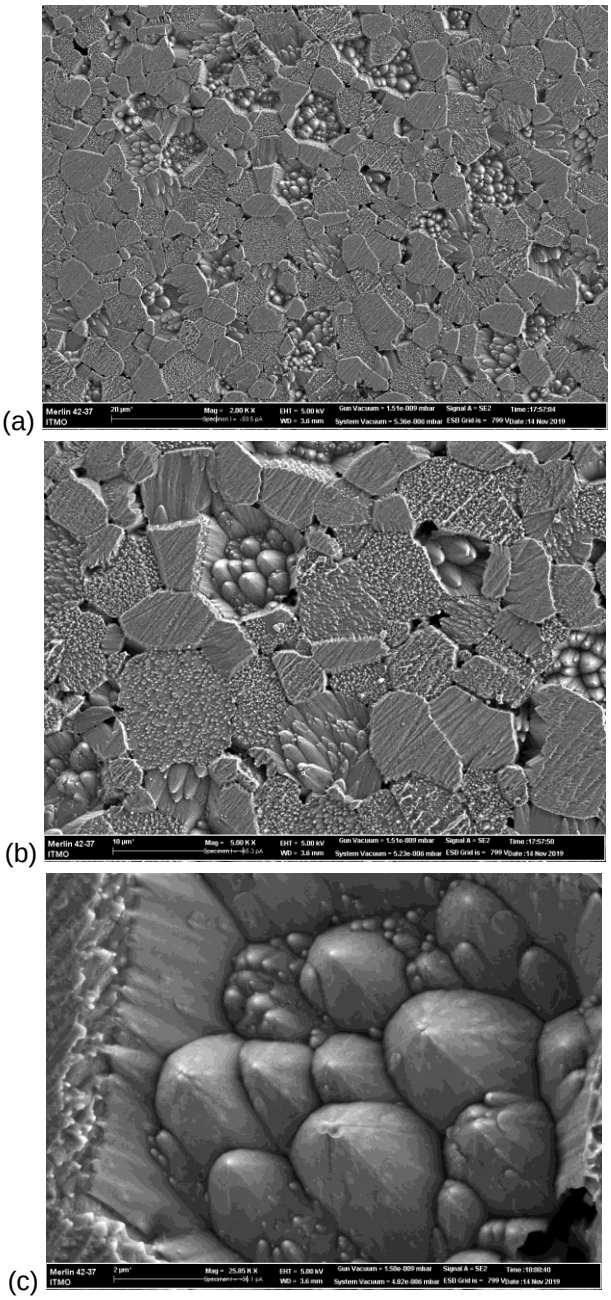

Figure 6. (a-c) Typical SEM images of the polished and etched surface of a 1.0 wt% Yb-doped ZnO ceramic fabricated at 1150 °C (Yb_2O_3 from batch No. 1). The scale bar is (a) 20 μm, (b) 10 μm and (c) 2 μm.

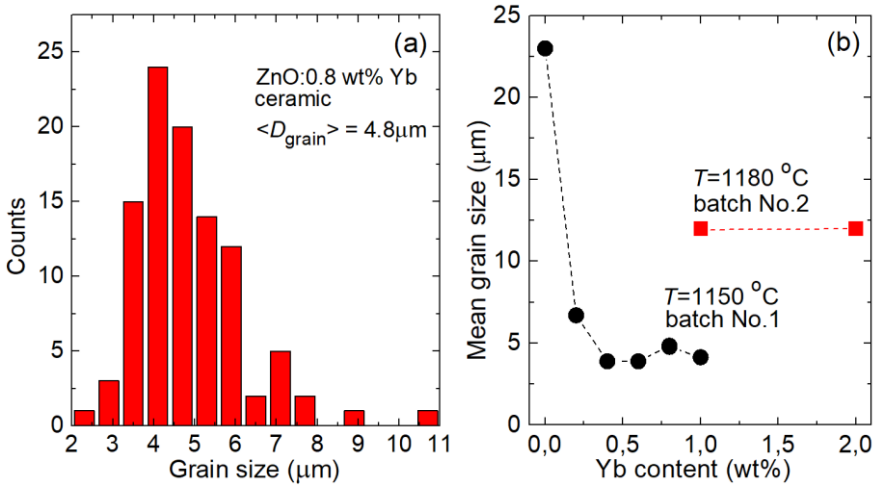

Figure 7. (a) Typical grain size distribution for the ZnO:0.8 wt% Yb ceramic sintered at 1150 °C; (b) variation of the average ZnO grain size determined from the SEM images as a function of Yb content.

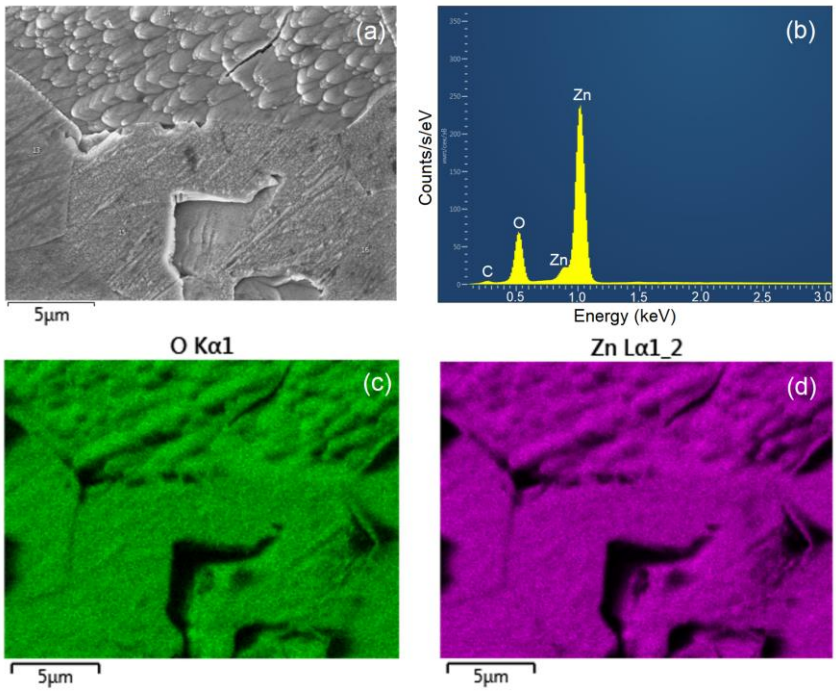

Figure 8. SEM-EDX analysis of undoped ZnO ceramic: (a) SEM image; (b) EDX spectrum (the whole area); (c,d) EDX-based element mapping: (c) O Kα1; (d) Zn Lα1,2.

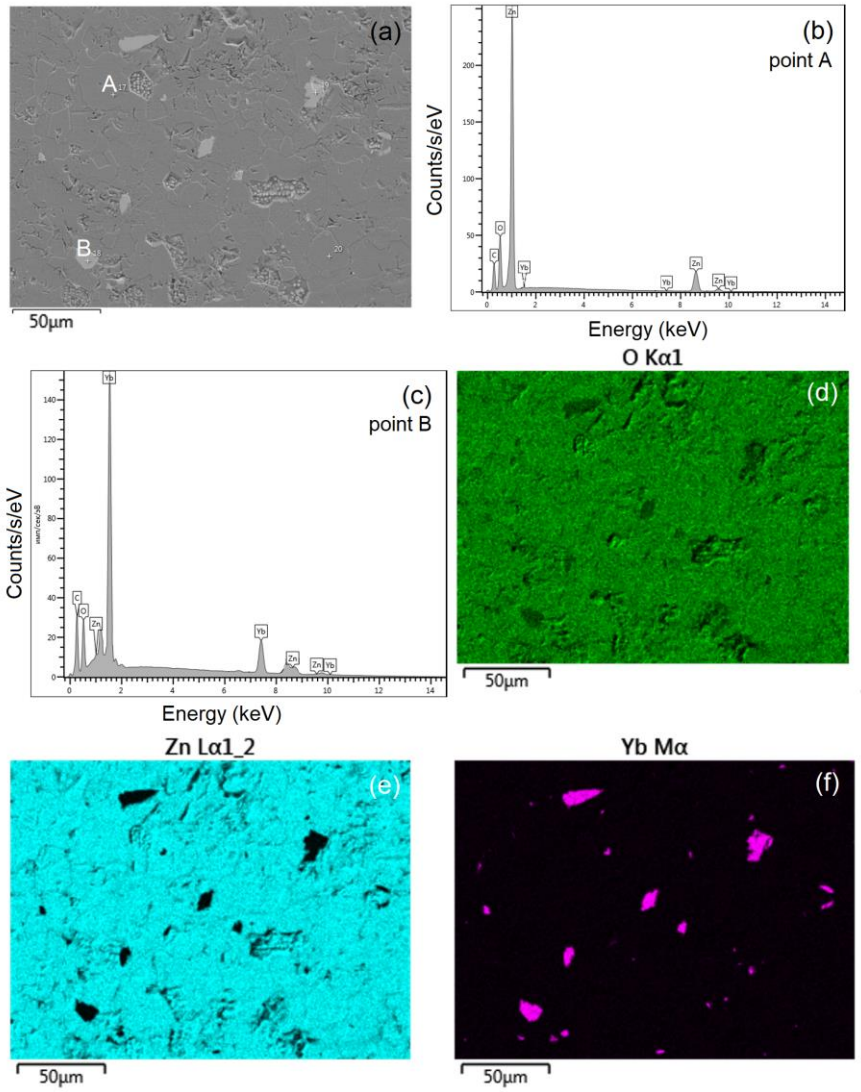

Figure 9. SEM-EDX analysis of ZnO:1.0 wt% Yb ceramic fabricated at 1180 °C: (a) SEM image; (b) EDX spectrum, point A; (c) EDX spectrum, point B; (d-f) EDX-based element mapping: (d) O Kα1, (e) Zn Lα1,2; (f) Yb Mα.

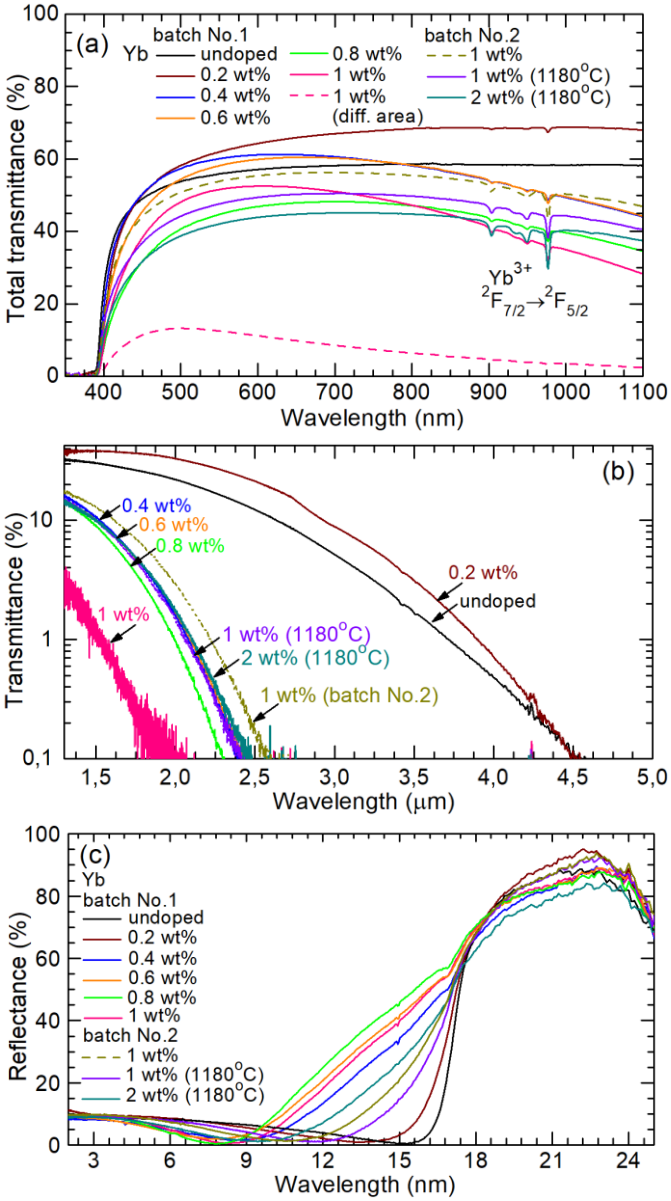

Figure 10. Transmittance and reflectance spectra of undoped and Yb-doped ZnO ceramics: (a) total transmittance spectra in the range of 350 – 1100 nm; (b) IR transmittance spectra in the range of 1.3 – 5 μm; (c) reflectance spectra in the range of 2 – 25 μm, "diff." means different. The sample thickness is ~0.5 mm.

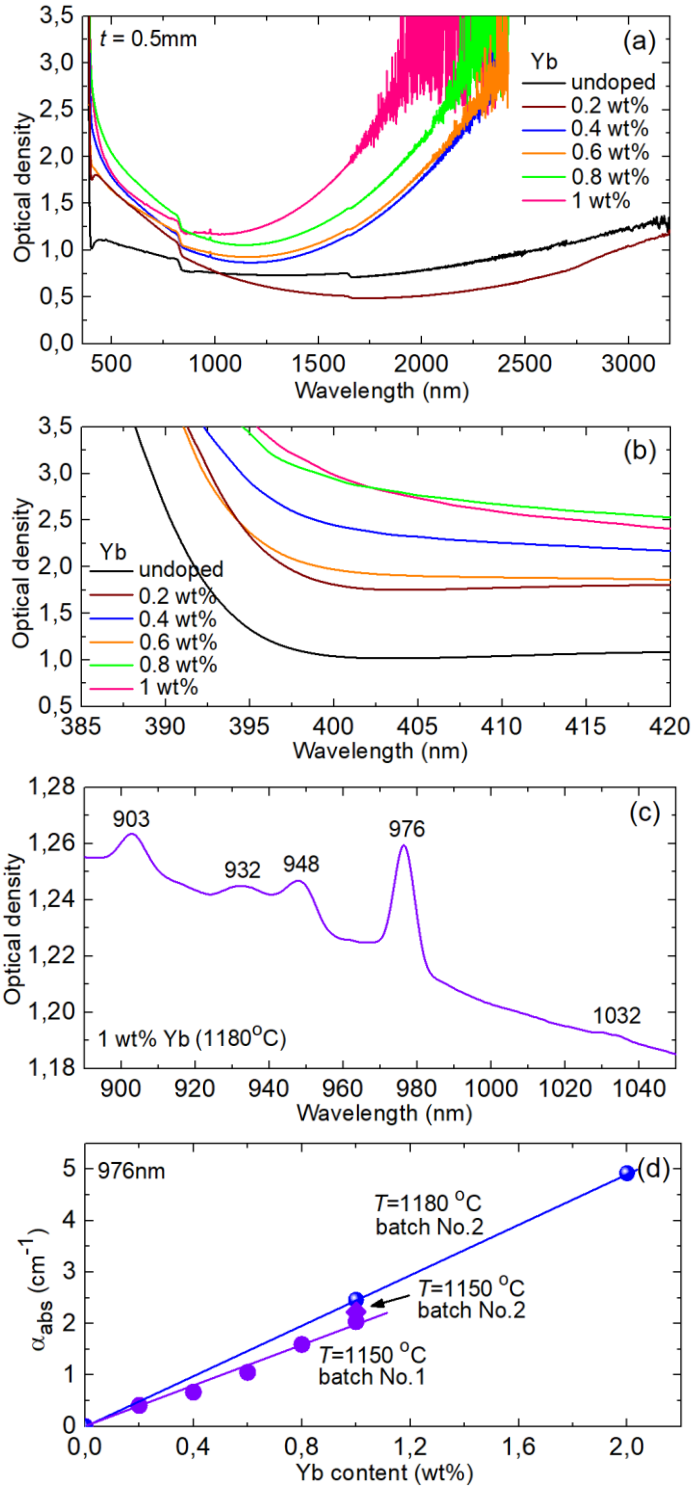

Figure 11. Absorption spectra of undoped and Yb-doped ZnO ceramics: (a,b) Yb_2O_3 from the batch No. 1, hot pressing temperature 1150 °C, (a) the spectral range of 360 - 3200 nm, (b) the spectral range of 385-420 nm; (c) absorption of Yb^{3+} ions at 890-1050 nm (ZnO:1 wt% Yb ceramic, batch No. 2, hot pressing temperature 1180 °C); (d) the dependence of the peak absorption coefficient at 976 nm on the Yb content. The sample thickness is ~0.5 mm.

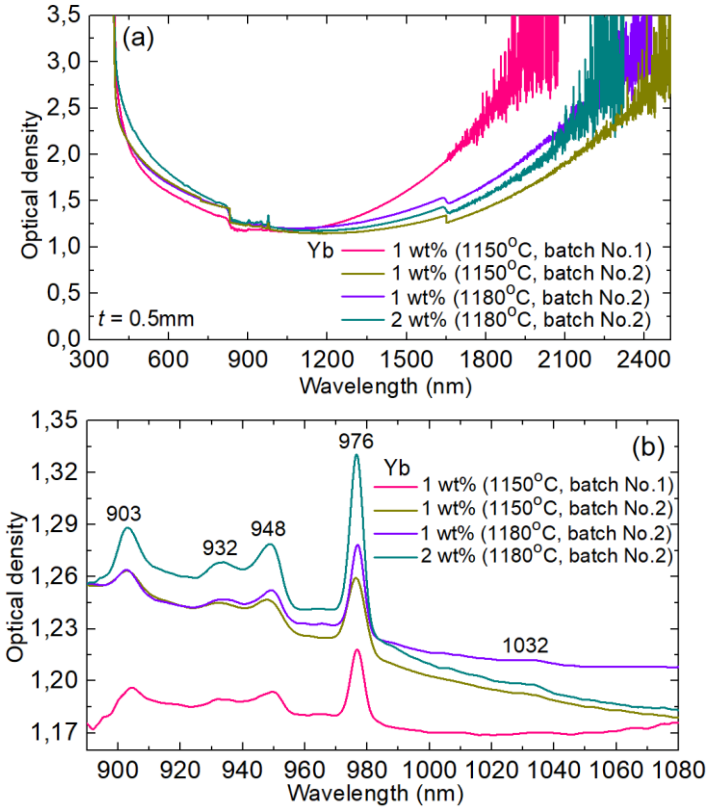

Figure 12. Room temperature absorption spectra of ZnO:1 wt% Yb ceramics fabricated at 1150 and 1180 °C and ZnO:2 wt% Yb ceramic fabricated at 1180 °C: (a) the spectral range of 300 - 2500 nm; (b) absorption of Yb^{3+} ions at 890-1080 nm. The sample thickness is ~0.5 mm.

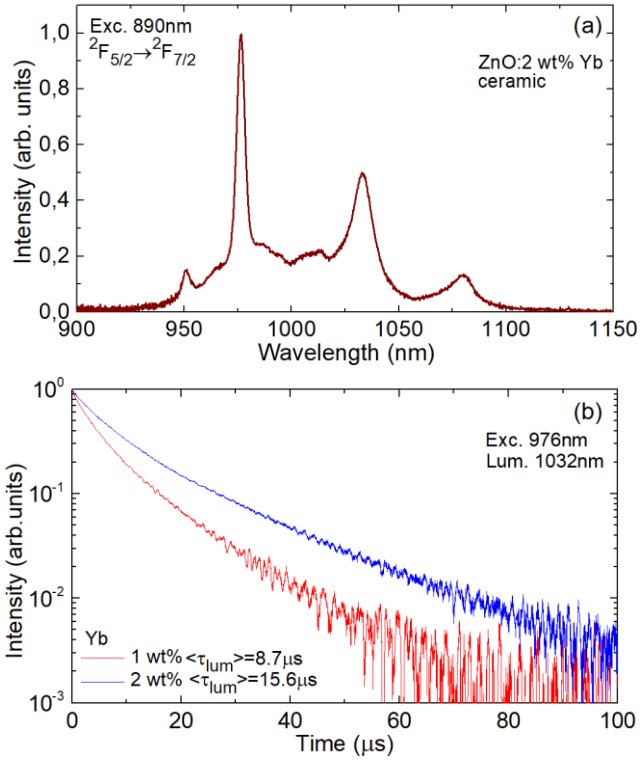

Figure 13. (a) RT luminescence spectrum of Yb^{3+} ions in the ZnO:2 wt% Yb ceramic fabricated at 1180 °C, λ_{exc} = 890 nm; (b) luminescence decay curves for ZnO:Yb ceramics with 1.0 and 2.0 wt% Yb, λ_{exc} = 976 nm, λ_{lum} = 1032 nm.

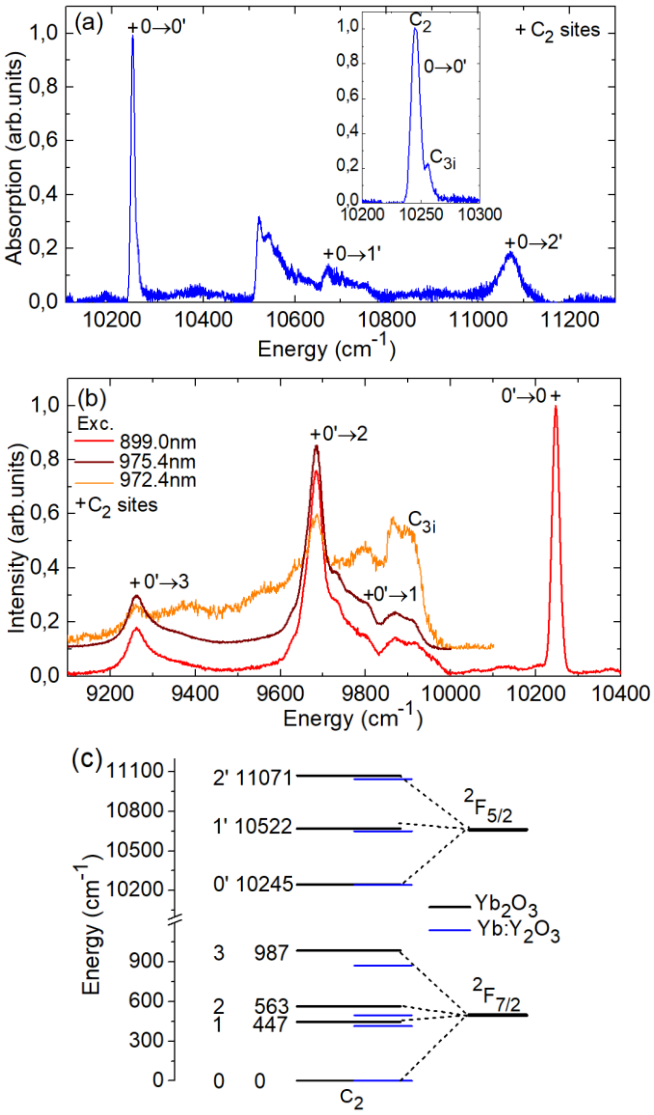

Figure 14. Low-temperature (10 K) (a) absorption and (b) luminescence spectra of Yb^{3+} ions in the ZnO:1 wt% Yb ceramic fabricated at 1180 °C, *inset* in (a) shows the zero-phonon line in absorption, "+" mark electronic transitions for Yb^{3+} ions in C_2 sites, C_{3i} – spectroscopic signatures of C_{3i} sites; (c) the scheme of energy-levels of Yb^{3+} ions in C_2 sites in the Yb_2O_3 crystals, the Stark splitting for Yb^{3+} ions in Y_2O_3 [81] is given for comparison.

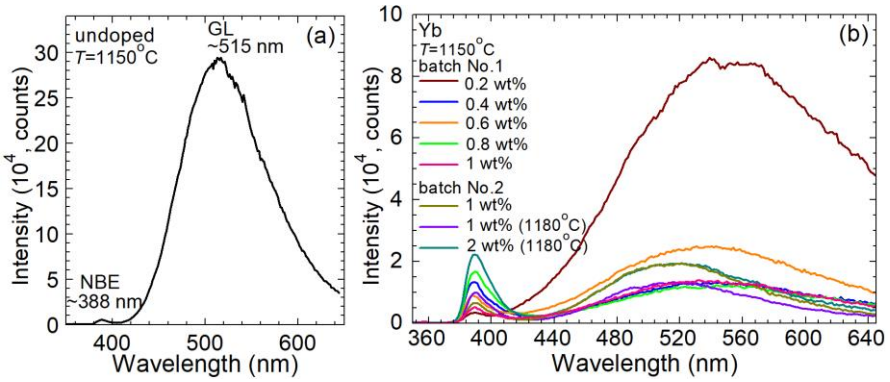

Figure 15. X-ray-induced luminescence spectra of ZnO and ZnO:Yb ceramics.

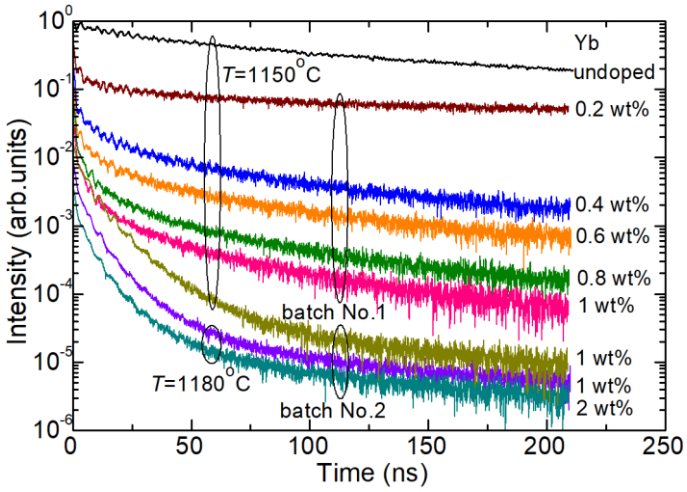

Figure 16. Decay kinetics of X-ray-induced luminescence of ZnO and ZnO:Yb ceramics. The *circle* marks the decay curves for ceramics fabricated at 1180 °C.

Table 1. Unit cell parameters of undoped and Yb-doped ZnO ceramics prepared at different hot-pressing temperatures.

Yb content, wt%	ZnO unit cell parameters (± 0.003 Å) *a*, Å	*c*, Å	Temperature of hot pressing, °C
undoped	3.250	5.204	1150
0.2	3.250	5.201	1150
0.4	3.251	5.203	1150
0.6	3.251	5.202	1150
0.8	3.252	5.203	1150
1.0	3.251	5.202	1150
1.0*	3.251	5.202	1150
1.0**	3.251	5.203	1180
2.0	3.251	5.202	1180

* - batch No. 1; ** - batch No. 2.

Table 2. Frequencies of the Raman-active modes of crystal phases as deduced from the measured high-resolution Raman spectra of ceramics in comparison with literature data.

Frequency, cm^{-1}						Symmetry	Process
This paper	[59]	[57]	[60]	[58]	[25]	[58]	[58]
99	101	101	101	99	98	E_2	E_2^{low}
204	208		208	203	200	A_1, (E_2)	2TA; 2 E_2^{low}
				284		A_1	B_1^{high} –B_1^{low}
331	334		332	333	331	A_1, (E_2, E_1))	E_2^{high} –E_2^{low}
378	380	380	380	378	377	A_1	A_1, (TO)
		395				Quazi-A_1 [57]	Quazi-A_1, (TO)
		398				Quazi-E_1 [57]	Quazi-E_1, (TO)
409	407	413	408	410		E_1	E_1 (TO)
437	437	444	437	438	437	E_2	E_2^{high}
				483		A_1	2LA
536			541	536		A_1	$2B_1^{low}$; 2LA
	574	579		574	580	A_1	A_1(LO)
		585	-			Quazi-A_1[57]	Quazi-A_1 (LO)
		585				Quazi-E_1 [57]	Quazi-E_1 (LO)
584	583	591	584	590		E_1	E_1 (LO)
				618		A_1	TA+TO
				657		E_1, E_2	TA+LO
663	Broad, 540 – 670		-	666		A_1	TA+LO
				700		A_1	LA+TO
				723		A_1	LA+TO
				745		A_1	LA+TO
				773		A_1	LA+TO
				812		A_1	LA+LO
	986			980		A_1	2TO
				1044		A_1	TO+LO
				1072		A_1	TO+LO
1096	Broad, 1084 (peak)			1105		A_1	2LO
1153	Broad, 1149 (peak)		1160	1158		A_1	$2A_1$(LO), $2E_1$(LO); 2LO

Table 3. Texture coefficients for planes of simple forms in undoped and Yb-doped ZnO ceramics prepared at the hot-pressing temperature of 1150 °C ([a]) and 1180 °C ([b]).

Miller's indices, *hkl*	Yb concentration, wt%							
	undoped[a]	0.2[a]	0.4[a]	0.6[a]	0.8[a]	1.0[a]	1.0[a*]	1.0[b*]
	Texture coefficient for planes of simple forms							
100	1.22	0.99	0.96	1.04	1.05	0.98	1.99	1.59
002	0.62	1.14	1.49	1.40	1.36	1.59	0.34	0.33
101	0.88	1.09	1.10	1.12.	1.11	1.09	1.35	1.21
102	0.76	1.18	1.29	1.27	1.20	1.33	0.76	0.73
110	1.29	0.99	0.92	0.95	0.97	0.92	1.73	1.32

*Batch No. 2.

Table 4. Characteristic decay times of X-ray induced luminescence decay characteristics of ZnO:Yb optical ceramics.

Yb content, wt.%	Yb_2O_3 batch	HPing temperature, °C	Decay time	
			τ_{fast}, ns	$\tau_{slow,}$ ns
0	-	1150	38	99
0.2	No. 1	1150	3.4	99
0.4	No. 1	1150	1.2	67
0.6	No. 1	1150	1.2	64
0.8	No. 1	1150	1.5	58
1.0	No. 1	1150	1.9	53
1.0	No. 2	1150	5.7	34
1.0	No. 2	1180	3.5	45
2.0	No. 2	1180	3.5	52